BRNO UNIVERSITY OF TECHNOLOGY

Faculty of Mechanical Engineering

MASTER'S THESIS

Brno, 2024 Bc. Jiří Spousta

BRNO UNIVERSITY OF TECHNOLOGY

VYSOKÉ UČENÍ TECHNICKÉ V BRNĚ

FACULTY OF MECHANICAL ENGINEERING

FAKULTA STROJNÍHO INŽENÝRSTVÍ

INSTITUTE OF PHYSICAL ENGINEERING

ÚSTAV FYZIKÁLNÍHO INŽENÝRSTVÍ

LOCALIZED OXIDATION OF VANADIUM FILMS ACCOMPANIED BY IN-SITU ANALYSIS

LOKALIZOVANÁ OXIDACE VANADOVÝCH VRSTEV DOPLNĚNÁ IN-SITU ANALÝZOU

MASTER'S THESIS

DIPLOMOVÁ PRÁCE

AUTHOR — Bc. Jiří Spousta

AUTOR PRÁCE

SUPERVISOR — Ing. Filip Ligmajer, Ph.D.

VEDOUCÍ PRÁCE

BRNO 2024

BRNO UNIVERSITY OF TECHNOLOGY
FACULTY OF MECHANICAL ENGINEERING

Assignment Master's Thesis

Institut:	Institute of Physical Engineering
Student:	**Bc. Jiří Spousta**
Degree programm:	Physical Engineering and Nanotechnology
Branch:	no specialisation
Supervisor:	**Ing. Filip Ligmajer, Ph.D.**
Academic year:	2023/24

As provided for by the Act No. 111/98 Coll. on higher education institutions and the BUT Study and Examination Regulations, the director of the Institute hereby assigns the following topic of Master's Thesis:

Localized oxidation of vanadium films accompanied by in–situ analysis

Brief Description:

The diploma thesis should explore localized oxidation processes on vanadium films in order to create vanadium dioxide (VO2) nanostructures. VO2 is a phase–change material that plays a pivotal role in various technological applications, ranging from tunable nanophotonics to "smart" windows. Localized oxidation of vanadium films can be used to imprint nanostructured VO2 textures into the films, which can then play a role of actively tunable components of integrated photonic circuits.

This thesis seeks to investigate the localized oxidation mechanisms of vanadium films and their evolution in real–time through in–situ analysis techniques. The work should begin by depositing vanadium films on substrates using ion–beam sputtering. Subsequently, localized oxidation should by initiated under controlled conditions (film thickness, temperature, gas environment,) by near–field illumination through an optical fiber. Various in–situ analysis techniques should be simultaneously utilized to observe the oxidation in real time (scanning electron microscopy, optical reflectance spectroscopy, atomic force microscopy). The obtained insights should not only contribute to the fundamental understanding of thin film oxidation but also have practical implications for the design of integrated tunable nanophotonic circuits.

Master's Thesis goals:

1) Deposition of films of vanadium and its oxides in different stoichiometries that will be suitable for localized modification (oxidation).
2) Performing localised modification (oxidation) under controlled conditions. Identification of key parameters of this process. Characterisation of the fabricated textures and nanostructures.
3) Implementation of in–situ control of the modification (oxidation) process.

Recommended bibliography:

SCHRECONGOST, Dustin; XIANG, Yinxiao; CHEN, Jun; YING, Cuifeng; ZHANG, Hai-tian et al. Rewritable Nanoplasmonics through Room-Temperature Phase Manipulations of Vanadium Dioxide. Online. Nano letters. 2020, roč. 20, č. 10, s. 7760-7766. ISSN 1530-6984. Dostupné z: https://doi.org/10.1021/acs.nanolett.0c03349.

SCHRECONGOST, Dustin; AZIZIHA, Mina; ZHANG, Hai-tian; TUNG, I-cheng; TESSMER, Joseph et al. On-Demand Nanoscale Manipulations of Correlated Oxide Phases. Online. Advanced functional materials. 2019, roč. 29, č. 49. ISSN 1616-301X. Dostupné z: https://doi.org/10.1002/adfm.201905585.

ZHANG, Hai-tian; GUO, Lu; STONE, Greg; ZHANG, Lei; ZHENG, Yuan-xia et al. Imprinting of Local Metallic States into VO2 with Ultraviolet Light. Online. Advanced functional materials. 2016, roč. 26, č. 36, s. 6612-6618. ISSN 1616-301X. Dostupné z: https://doi.org/10.1002/adfm.201601890.

Deadline for submission Master's Thesis is given by the Schedule of the Academic year 2023/24

In Brno,

L. S.

prof. RNDr. Tomáš Šikola, CSc. Director of the Institute	doc. Ing. Jiří Hlinka, Ph.D. FME dean

ABSTRACT

This diploma thesis deals with development and application of a unique method of locally oxidizing vanadium-based thin films inside the vacuum chamber of a scanning electron microscope. For this purpose, we use photonic crystal fiber to bring both O_2 gas and intense laser light ($\lambda = 532\,\mathrm{nm}$). After several iterations of finding the optimal configuration for the local modification on the vanadium-based sample surface (single-fiber or dual-fiber version of the method), the configuration deemed most suitable involved bringing a planar photonic crystal fiber, attached to the LiteScope AFM microscope tuning fork from NenoVision, close to the sample surface in a precise manner. Close sample surface-AFM probe proximity and sufficient flow of O_2 molecules lead to a successful local modification of oxidation state in the thin vanadium-based film. The thesis also describes results obtained by measuring Raman fingerpints of locally modified (oxidized) regions, that prove our novel approach of local oxidation successful and open new fabrication procedures of vanadium oxides.
The work also contains descriptions of the necessary modifications made to the SEM to accommodate the experimental setup for local oxidation (multifunctional gas injection system), along with details on the fabrication process of thin vanadium-based films by IBAD.

KEYWORDS

vanadium dioxide, ion beam assisted deposition, local oxidation, AFM, SEM, Raman spectroscopy

ABSTRAKT

V předložené diplomové práci se zabýváme popisem a aplikací námi vyvinuté metody lokální oxidace vanadových vrstev v komoře elektronového mikroskopu. K tomuto účelu používáme duté optické vlákno, které na zvolené místo na povrchu vzorku může přivést jak pracovní plyn (O_2), tak i intenzivní laserové světlo ($\lambda = 532\,\mathrm{nm}$). Po několika iteracích hledání nejvhodnější konfigurace lokálního ovlivňování povrchu vanadu (jednovláknová, případně dvouvláknová verze metody) byla jako nejvhodnější vyhodnocena varianta, ve které bylo planární duté optické vlákno (připevněné k ladičce AFM mikroskopu LiteScope od firmy NenoVision) definovaným způsobem přiblíženo k povrchu vanadové vrstvy. Blízkost povrchu a dostatečný tok pracovního plynu kapilárami dutého vlákna vedly k tomu, že se nám vanadovou vrstvu úspěšně podařilo zoxidovat. V práci jsou rovněž popsány výsledky měření Ramanovy spektroskopie takto lokálně ovlivněných vanadových vrstev, které ukázaly, že zvolená metoda, kterou jsme objevili, byla úspěšná a otevírá nové možnosti přípravy tohoto zajímavého materiálu.
V práci jsou rovněž uvedeny a popsány nezbytné konstrukční úpravy stávající experimentální sestavy pro lokální oxidaci (multifunkčního systému vstřikování plynu) a popis přípravy tenkých vanadových vrstev metodou IBAD.

KLÍČOVÁ SLOVA

oxid vanadičitý, naprašování iontovým svazkem, lokální oxidace, AFM, SEM, Ramanovská spektroskopie

SPOUSTA, Jiří. *Localized oxidation of vanadium films accompanied by in-situ analysis*. Brno: Brno University of Technology, Faculty of Mechanical Engineering, Department of Physical Engineering, 2024, 55 p. Master's Thesis. Supervised by Ing. Filip Ligmajer, Ph.D.

Author's Declaration

Author:	Bc. Jiří Spousta
Author's ID:	220467
Paper type:	Master's Thesis
Academic year:	2023/24
Topic:	Localized oxidation of vanadium films accompanied by in-situ analysis

I declare that I have written this paper independently, under the guidance of the advisor and using exclusively the technical references and other sources of information cited in the paper and listed in the comprehensive bibliography at the end of the paper.

As the author, I furthermore declare that, with respect to the creation of this paper, I have not infringed any copyright or violated anyone's personal and/or ownership rights. In this context, I am fully aware of the consequences of breaking Regulation § 11 of the Copyright Act No. 121/2000 Coll. of the Czech Republic, as amended, and of any breach of rights related to intellectual property or introduced within amendments to relevant Acts such as the Intellectual Property Act or the Criminal Code, Act No. 40/2009 Coll. of the Czech Republic, Section 2, Head VI, Part 4.

Brno ....

author's signature*

*The author signs only in the printed version.

Nejprve bych rád poděkoval svému vedoucímu Ing. Filipu Ligmajerovi, Ph.D., za odborné vedení práce a cenné rady.

Moje další díky patří Ing. Zdeněku Nováčkovi, Ph.D., Ing. Martinu Konečnému, Ph.D., za pomoc a rady zejména při vývoji metody lokální oxidace a za všechen smích a veselí, které jsme při tom zažili. Děkuji také doc. Ing. Petru Báborovi, Ph.D., za pomoc s vakuovou technikou a Ing. Stanislavu Vobornému, Ph.D., za půjčení hmotnostního spektrometru a doc. RNDr. Miroslavu Doložílkovi, CSc., za zapůjčení jediného notebooku na světě, se kterým hmotnostní spektrometr komunikoval.

Děkuji rovněž Ing. Jaroslavu Kubíčkovi z Ústavu strojírenské technologie FSI za bleskové svaření vakuového systému vstřikování plynu. Velké díky patří celému Ústavu fyzikálního inženýrství, hlavně prof. RNDr. Tomáši Šikolovi, CSc. za atmosféru, jakou vytvořil a vytváří, za možnost výjezdu na Erasmus a za veškerou nezištnou práci, kterou pro nás, studenty, dělá. Děkuji také mé rodině, která při mně zejména ke konci stála a poskytovala potřebné zázemí a mé přítelkyni Káje, která to se mnou tento závěrečný školní rok neměla lehké a zvládla to velmi statečně.

Děkuji kamarádům a spolužákům za podporu. Didovi za práci na fréze a za to, že mě celou dobu vtipem a hláškami z Červeného trpaslíka držel nad vodou. Pavlovi, že mě vzal na zásadní měření Ramana dva dny před odevzdáním této práce a vůbec za to, jak nedílnou součástí mé širší rodiny se stal.

Tato práce byla provedena za podpory výzkumné infrastruktury CzechNanoLab (ID LM2023051, MŠMT, 2023–2026), CEITEC Vysoké učení technické v Brně. Tato práce byla z části podpořena projektem INCHAR (FW03010504 Vývoj in-situ technik pro charakterizaci materiálů a nanostruktur) se státní podporou Technologické agentury ČR v rámci programu TREND.

CONTENTS

INTRODUCTION

Vanadium dioxide is a material of significant interest due to its metal to insulator phase change occuring at only 67 °C. Such material can be used to create tunable optical metasurfaces, an optical element made of building blocks with sizes below diffraction limit with more than one functionality. This multifunctional effect of a singular optical element as well as incredible wavefront manipulations made possible when using an optical metasurface, such as negative refractive index and invisibility cloaking, is unprecedented in traditional optics.

Traditionally, VO_2 is made by globally annealing vanadium-based samples, however any inhomogeneities introduced during the sample fabrication are imprinted during the global anneal process. We therefore obtain several parasitic vanadium oxide stoichiometries in a single sample, with local regions providing different. Also, when fabricating a structured VO_2 sample, different structural geometries require different annealing parameters, restricting us to one optimization cycle per annealing process an inefficient way of dealing with lithographically obtained samples. Locally controlling the oxidation process would mean more efficient structured sample fabrication. Also, since the oxidation parameters are heat and O_2 intake in both local and global oxidation schemes, a primary estimate of sample behaviour when exposed to concrete parameters could be quantified prior to global annealing, when several samples of the same geometries at once need to be fabricated. Another benefit of local oxidation of a vanadium sample would be overall bypass of lithography, in some cases. If we could locally imprint suitable geometries of various vanadium oxides we could achieve similar results, without the necessity of all time consuming steps connected to lithography (mask deposition, resist coating, etching...).

One such method of locally controlling sample oxidation states is local anodic oxidation (LAO). LAO works by breaking water molecules near a sharp AFM tip by high electric field strengths near the tip. LAO therefore requires a ambient humidity, which is difficult to achieve in a vacuum chamber. Along with necesarry humidity, the sample surface modification using the LAO method is dependent on sample surface conductivity. This is one of the possible reasons for why LAO of vanadium-based samples has been published for the first time in 2022.

In this diploma thesis, we focused on development, implementation, and characterization of a novel local oxidation method. The cornerstone of our local oxidation method is bringing two crucial oxidation parameters, heat (induced by laser light) and O_2 gas in a defined manner into the vacuum chamber of a scanning electron microscope. We have decided to implement both of these oxidation parameters by photonic crystal fibers, that can bring both laser light and gas due to their waveguiding core surrounded by thin capillaries. We have manipulated these photonic crystal fibers by either LiteScope AFM-in-SEM module, allowing for topography measurements of modified regions along with SEM imaging, or by a vacuum fiber micromanipulator. Both of these fiber manipulators are precise enough to form local oxidation sites of well defined geometries on our

vanadium-based thin films. Locally modified regions were subjected to optical characterization by Raman spectroscopy, a method capable of determining any oxidation state changes we have induced during local oxidation.

1 SAMPLE PREPARATION AND ANALYSIS

In this chapter we will discuss vanadium and vanadium oxide based sample preparation and their subsequent analysis. First section is dedicated to Ion Beam Assisted Deposition using a Kaufman type ion source. The following parts various possible oxidation processes. Lastly optical characterization using Raman spectroscopy of vanadium oxides is discussed, with prior work in this field shown.

1.1 Ion Beam Assisted Deposition

Ion beam assisted deposition (IBAD) is a physical vapor deposition technique. IBAD operational principle starts by creating (and sustaining) plasma inside the primary ion source chamber. Our deposition apparatus is based on a Kaufman type ion source [1], which was originally designed for spacecrafts. This part was written using information found in the literature [2], most notably the operational principle of the Kaufman type ion source.

In Kaufman ion sources, electrons are extracted from a hot tungsten cathode (filament) and fly towards an anode through the primary ion chamber. By continuously injecting Ar atoms into the primary ion chamber via a gas inlet we ensure collisions between electrons and atoms. The most probable outcome of the collision is the Ar atom losing an electron. This collision event therefore yields another anode-bound electron, that can ionize other Ar atoms, and an Ar^+ ion going in the opposite direction (towards the cathode).

The anodes of our deposition system are within magnetic fields generated by permanent magnets. These fields increase the probability of electron-atom collisions by elongating the path electrons must traverse before reaching the anode, therefore ensuring a more compact plasma creation. Due to the charge separation and difference in masses, an attractive Coulomb force is induced between the electrons and ions, forming a neutral

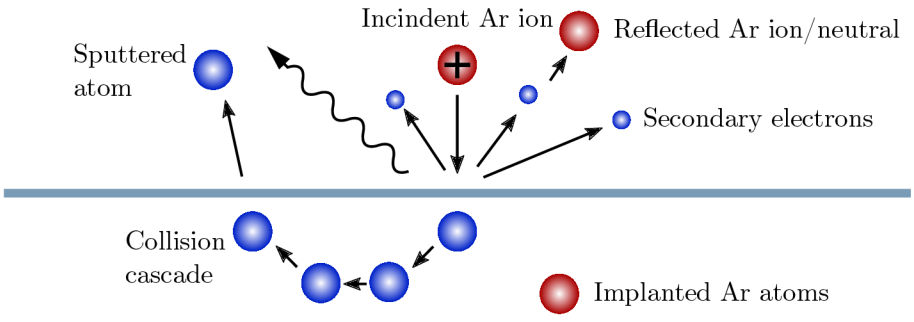

Fig. 1.1: Possible outcomes of an Ar ion/sample surface collision event. Incident Ar ion can be reflected or transfer its energy to the sample surface. This energy transfer can produce a secondary electron or via a collision cascade a sputtered atom. If the charged particle decelerates, a photon is emitted. The impinging particle can be implanted by penetrating into the sample.

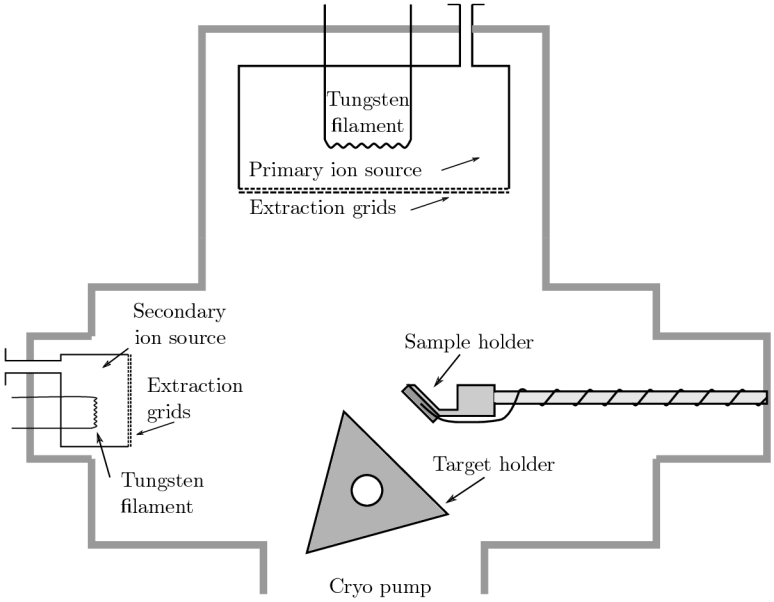

Fig. 1.2: Schematic of IBAD apparatus Kaufman. Ar^+ ions extracted from primary ion source chamber are focused onto V target surface. O_2 molecules flow out of secondary ion source chamber inlet and form a suitable atmosphere inside the deposition chamber. A specialized sample holder with pBN heating element and thermocouple enables controlled *in situ* annealing of vanadium oxide thin films.

plasma. We then increase the potential energy of created ions to 600 eV and extract them towards a grounded target using a negative potential on an extraction grid. The number of ions extracted can be roughly quantified by the current flowing in the extraction grid circuit.

Once the incident ion interacts with the target surface, a collision event occurs. This event can have multiple outcomes depending on the primary energy E_0, mass, incident angle of incoming ions, and binding energy of target atoms. For small binding energy of target atom values of E_0, the ion can be reflected. For high E_0 values, gas ions can be implanted into the target in the form of neutral atoms. Ions with higher mass have higher probability of ejecting atoms from the surface. This ejection is known as sputtering. The target atoms can be sputtered by Ar ions directly, when the mass of target atoms is much smaller than mass of the incident ions. This is typically not the case since target atoms are usually heavier, so a collision cascade tends to preceed possible surface atom sputtering. In that case, the Ar ion transfers its momentum to a surface atoms in a number of collision events, possibly leading to ejection of the last atom in the collision cascade, as illustrated in **Fig.** 1.1. Sputtered particles can also be charged, positively charged particles are unlikely to escape the target due to potential difference, and negatively charged particles are unlikely to even exist due to the collision nature. The incident ion can also excite atoms to generate secondary electrons. The secondary electron hitting an anode is from a current measurement standpoint the same as when a cathode is hit by the ion. Therefore, to ensure we measure the current of ions, not

electrons, a shielding grid is employed to absorb secondary electrons generated during collision events. Secondary ions can also emit characteristic photons. Characteristic X-ray photons can also be generated, potentially damaging delicate substrates (such as resist covered samples for lithography). For thin film deposition, the most desirable outcome is naturally to have as many sputtered particles as possible. The ratio between sputtered target particles and incident ions, i.e. how many ions must collide with the target to create one sputtered target particle, is called sputtering yield. Sputtering yield (for many materials this is a tabulated value [3]) correlates to sputtering rate, which represents how fast a thin layer grows, materials with higher sputtering yield have a higher sputtering rate.

One of this diploma thesis goals was to prepare vanadium-based thin films. We sputtered using Ar^+ ions and a 99% pure vanadium target. Pressure inside the deposition chamber (see **Fig.** 1.2) varied depending on the Ar flow, but was usually equal to $5 \cdot 10^{-4}$ mbar. This combination yielded metallic vanadium thin films prepared on fused silica and crystalline silicon. To grow layers consisting of vanadium oxides, we have employed the secondary ion chamber of IBAD apparatus Kaufman. Using the secondary gas inlet, we created an O_2 atmosphere within the deposition chamber. This process ensured that after being adsorbed onto the sample surface, sputtered vanadium particles reacted with O_2 atoms, resulting in the formation of vanadium oxide molecules of various stoichiometry that subsequently create thin films. Lastly, for growing VO_2 thin films, *in-situ* annealing was employed. For this purpose, a pBN heating element was used and implemented via a modified sample holder and an adapter (see **Fig.** 1.3). When elec-

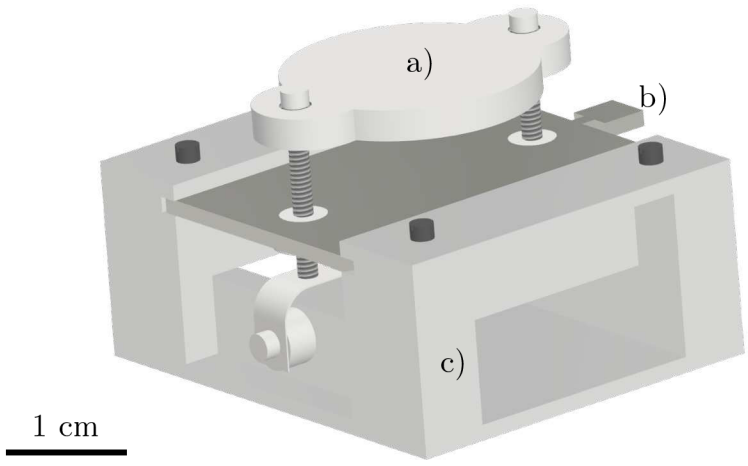

Fig. 1.3: Custom made sample holder. A pBN heating element (a) enables *in situ* heating. Conductive copper screws connect the heating element to a palette (b). The palette is connected to a sample holder (c) allowing for easy removal of samples after sample fabrication. Designed using the Autodesk Inventor tool.

tric current flows through the pBN heating element, its temperature rises and the layers growing on top of the sample can be annealed. To ensure a well-defined control of temperature, the sample holder was further modified to accomodate a k-type thermocouple. The pBN heating element increases its temperature up to 1400 °C in vacuum if electric current passes through. To use the pBN heater surface as a sample holder, a custom palette was made out of stainless steel (as seen in **Fig.** 1.3). We used copper screws to fix the heating element onto the palette to achieve optimal conductivity. This palette can be simply inserted into a special holder with integrated flaps designed to connect the pBN heating element with two copper wires. Using a power feedthrough, these wires are then led outside the deposition chamber into a laboratory DC voltage source.

1.2 Vanadium oxide sample modification

A crucial part of vanadium oxide sample fabrication process is introducing the sample to heat. If we provide the correct amount of energy, not only can we change the outcome of sample fabrication in our favor, we will also obtain a crystalline structure. There are two possible ways of sample annealing, depending on when annealing takes place. We can anneal after the growth has finished (*ex situ*) [4]. This approach, while viable, has several disadvantages. Different sample parameters (e.g. thin film thickness, nanoparticle size etc.) must have customized annealing parameters (typically temperature and oxygen flow), so thorough and lengthy optimization follows for every new parameter. Still, sample fabrication using *ex-situ* sample modification is often utilized, as we will see below. However, for VO_2 samples, the established approach of fabrication typically utilizes annealing during growth (*in-situ*). While *in-situ* annealing requires optimization of annealing parameters similar to the *ex-situ* counterpart, one iteration should suffice for multiple sample parameters (until drastic differences of sample thicknesses are involved). For VO_2 possible thin film deposition methods are chemical vapor deposition [5], pulsed laser deposition [6], magnetron sputtering [7] and each of these methods can incorporate *in-situ* annealing.

1.2.1 Annealing

Vanadium is a transition metal element with several valence states. For its VO_2 stoichiometry, vanadium is in V^{4+} valence state. It is common [8] to oxidize other similar compositions (e.g. V_2O_5, V_3O_7...), who may not exhibit [9] the same change in its properties VO_2 is known for [10]. This effect of impurities oxidizing during growth can be corrected by sample annealing, as stated in the paragraph above. By annealing the sample in an O_2 atmosphere we can modify its stoichiometries. A similar approach has been established to reduce vanadium oxide samples aswell. In [11], a hydrogen reducing atmosphere was employed to reduce V_2O_5 back all the way to VO. Both approaches act upon the entire sample surface. Local modifications of the sample are therefore not possible, greatly prolonging the fabrication process of for example structured vanadium oxide samples. As either e-beam or light lithography are the usual methods of choice for structured sample fabrication, one sample would preferrably contain multiple arrays of structures. Per one nanostructured sample, only one iteration of annealing parameters can be done, greatly limiting the yield and increasing time needed for optimization. Along with nanostructured samples, several deposition methods suffer from slightly inhomogeneous thin film growth. For example, due to faster growth rates during ion beam sputtering [12] (as opposed to slower, but more homogeneous thin film growth methods such as molecular beam epitaxy [13]), differently oriented grains are formed into islands (hence island growth). Annealing affects the entire sample.

1.2.2 Anodic oxidation

Another approach of obtaining vanadium oxides can be anodic oxidation [14]. Anodic oxidation utilizes electrochemical processes to accelerate oxidation phenomena. The most direct experimental setup consists of two electrodes connected to a voltage source, submerged in a suitable electrolyte. When electric current is passed through the system, hydroxyl radical are formed inside the electrolyte allowing for strong oxidation of the anode. When vanadium oxides are considered, it was shown that a crucial oxidation parameter is the formation of V^{4+} and V^{5+} ions [15]. The ratio between these two types ions can be controlled by the applied voltage, determining the product of the oxidation. While the growth product can be easily monitored by employing *in situ* characterization of deposited thin films, the oxidation structure was complex. Due to results varying from porous layers to nanowire growth, this approach was set aside by the scientific society and conventional annealing is now the go to method for vanadium oxide based sample fabrication. Perhaps a more localized approach of electrochemical oxidation in local anodic oxidation would not suffer from such inhomogeneous growth properties.

1.2.3 Local Anodic Oxidation

Local anodic oxidation (LAO) has recieved renewed interest mainly for its versatility. The method itself is based upon conductive Atomic Force Microscopy, c-AFM. In c-AFM, a voltage bias is applied between the sharp tip of an AFM probe and sample surface, allowing for measurements of current flow as well as topography to be done. LAO adds water meniscus between the tip and the surface. The electric field strength (for 10 V bias and the probe in contact mode) formed near the tip of the AFM probe is:

$$V = Ed \propto 10^9\,\mathrm{V/m}, \tag{1.1}$$

where V is the voltage applied and d is the distance between the tip and the sample. Such fields can dissociate the water molecule inside the water meniscus into H^+, resp. OH^- ions that come onto the cathode (tip), resp. anode (surface). As well as dissociating water, surface atoms get ionized and drift into the meniscus, allowing for oxidation of the sample surface. This enables localized sample surface modifications. By increasing the voltage bias we can influence the thickness of the formed oxide structure [16]. Traditionally, this relation is linear, with an upper limit set by applied electric field power needed to eject atoms from the surface altogether. Another important parameter is the oxidation atmosphere humidity. Article [17] has shown that the relation between atmosphere humidity and geometrical properties of obtained oxidation sites is not linear. Rather, for lower humidity values (near 50%) the meniscus significantly varies in size over the experiment. This effect highlights the importance of a suitable experimental setup, while basic LAO experiments are possible even at lower humidities.

LAO has numerous similarities to our newly proposed local oxidation approach (as will be shown in Section 2). Both methods rely on an atomic force microscope bringing

a probe in close surface vicinity. Both methods also require a suitable oxidation atmosphere. LAO has difficulties working with non conductive samples due to its c-AFM nature [18]. Our novel method requires only for the sample to absorb a portion of light selected to bring energy to oxidation site. The light source can be tailored for distinct samples, greatly increasing its usability and versatility. In recent work, the first local

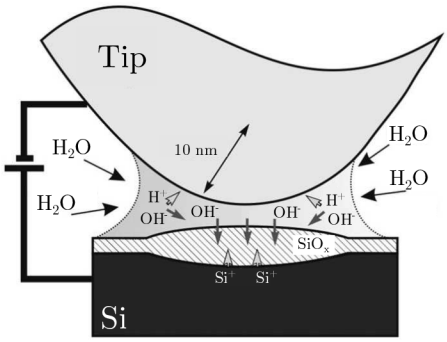

Fig. 1.4: Local anodic oxidation of silicon. Adapted from [19].

anodic oxidation of a vanadium-based thin film was presented [20]. Here, a demonstrated height increase induced by a sharp c-AFM tip served as proof of V^{4+} to V^{5+} oxidation change. The nanolithographical approach of thin vanadium-based films therefore needs further characterization since the field has not been explored in depth.

1.2.4 Laser-assisted oxidation

Laser assisted oxidation of vanadium thin films has been recently demonstrated as an effective way of locally controlling oxidation states of vanadium, with summarizing work published in 2023 [21]. Of six known attempts at locally oxidizing vanadium-based thin films, only two published (2017 and 2023) articles have demonstrated their experimental setup. In [22] a pre-structured vanadium dumbbell shape on quartz was locally oxidized using a focused laser. The laser light power was 40 mW, wavelength $\lambda = 532$ nm and spotsize 10 µm. The experiments were done in ambient conditions, relying on oxygen located in atmospheric pressure to supply local change of oxidation state. The affected dumbbell shapes were inhomogeneously etched, hinting at insufficient amount of oxygen species present in the local oxidation vicinity. Even though, a mixed phase of VO_2 and V_2O_5 locally induced changes were measured using Raman spectroscopy.

In [21], a lithography-free variant was presented. Here, a thin pristine vanadium film on a quartz substrate was modified using direct laser writing. The laser light power was 246 mW, wavelength $\lambda = 532$ nm. The research group underwent a study of suitable laser working distances (corresponding to laser spotsize) and exposure times. The optimal laser light spotsize on the sample surface was found in the focal point with the most compact modified point being around 100 µm in diameter. The experiments were done again in ambient conditions with possible modification to employ a controlled gas atmosphere hinted in the conclusions. The affected regions changed their stoichiometry to both VO_2 and V_2O_5, with oxidation states and morphology depending on the exposure time. For exposure times below 2.5 s, the modified area contained several cracks. For exposure times above 5 s the modification area contains grains but is more homogeneous, with VO_2 oxidation state obtained at 10 s and V_2O_5 oxidation state obtained at 100 s exposure time. These local changes were again characterized using Raman spectroscopy.

In [23], a local stoichiometry change from VO_2 to V_2O_5 occured during high power laser use in Raman spectroscopy. Using $\lambda = 632.8$ nm laser light power at 0.3 mW initially showed VO_2 Raman fingerprint, once the laser power output increased to 2.8 mW, the Raman spectrum was that of pure V_2O_5. This change was irreversible, as going back to initial laser light power at the modified region once again showed V_2O_5 Raman spectrum. This reaction is provoked by oxygen in the surrounding atmosphere and local heating caused by absorption of light. In the article, the temperature increase induced on the sample surface by the laser light was computed by an approximate relation (taken from [24]):

$$T = T_0 + P/(\kappa r(8\pi)^{1/2}), \tag{1.2}$$

where T is induced temperature, T_0 is ambient temperature, P is laser power, r is laser spot radius, and κ is thermal conductivity. For VO_2, $\kappa = 65\,\mathrm{mWcm^{-1}K^{-1}}$ [25], (for pure vanadium, a frequently used sample material in this thesis, $\kappa = 65\,\mathrm{mWcm^{-1}K^{-1}}$ [26]). The estimated VO_2 temperature during laser power output 2.8 mW was 300 °C.

1.3 Optical characterization of vanadium oxide samples

This section is dedicated to the theoretical background of methods used within the scope of this thesis for optical characterization of vanadium-based thin films. The first part is dedicated to Raman spectroscopy of various vanadium oxides we have came across during our work. We have used Raman spectroscopy to characterize especially the local changes of thin vanadium-based films.

1.3.1 Raman spectroscopy

Vanadium oxides have been studied due to its interesting physical properties [28]. The typical method of sample characterization being X-ray photoelectron spectroscopy [29] or Raman spectroscopy [30]. We have chosen the latter method to characterize our local oxidation endeavors. The principle of Raman spectroscopy is based upon inelastic scattering of monochromatic light. Such inelastic scattering can happen by energy transfers between the incident light and electronic transitions [31], molecular vibrations [32] or rotations [33]. We can then detect the scattered light and measure the energy shift corresponding to each inelastic mode. In Raman spectra we distinguish between Stokes or anti-Stokes energy shift. Stokes shift happens when a molecule is in ground state and a portion of incident

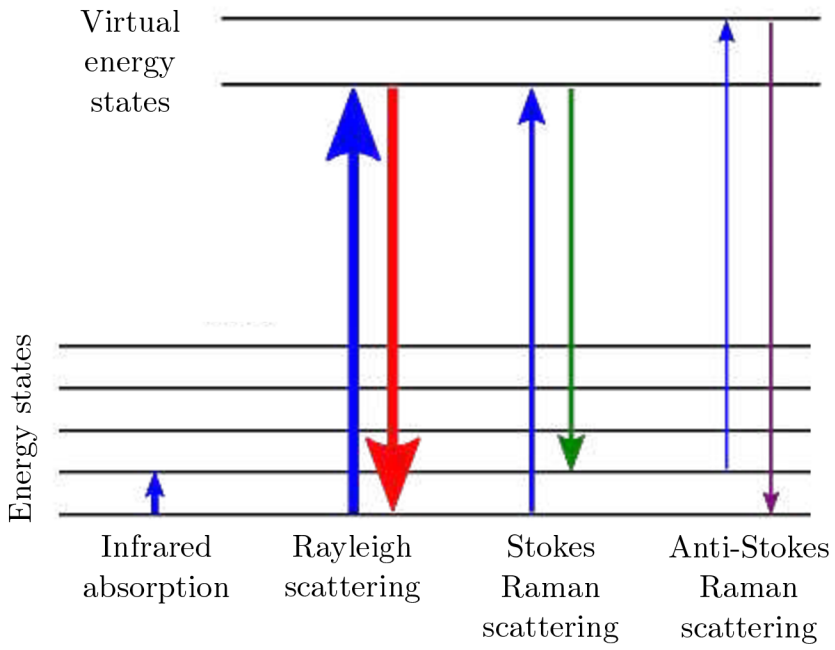

Fig. 1.5: Energy diagrams of elastic and inelastic scattering of light on a sample. Adapted from [27]

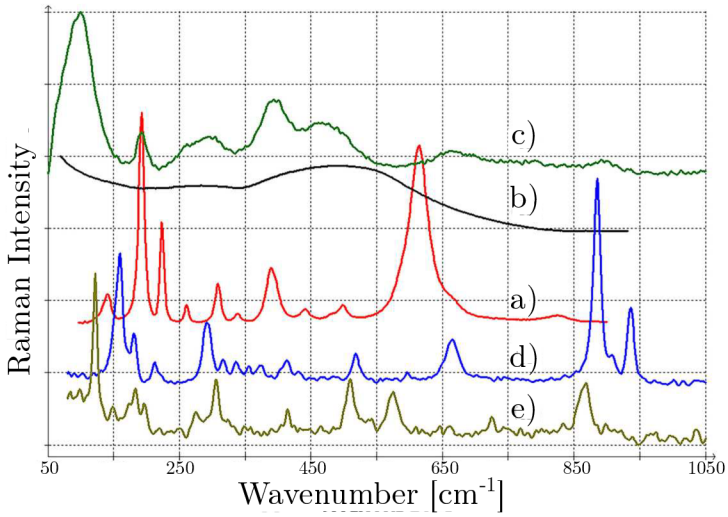

Fig. 1.6: Raman spectra of various VO_2 phases adapted from [34]. a) VO_2 in M1 phase measured in [35], b) VO_2 in rutile phase measured in [36], c) VO_2 (B) [37] and VO_2 tetragonal [38] phase measured at d) 30 °C and e) 200 °C.

photon energy is absorbed to excite the atom. The detected photon then has longer wavelength than the incident (lower energy). Anti-Stokes shift happens when a molecule is in an excited state and transfers its energy to the incident photon, dropping back to the ground state. The detected photon then has shorter wavelength (higher energy). Third possible outcome is elastic scattering, often called Rayleigh scattering. These three interactions are often displayed in energy level diagrams (see **Fig.** 1.5). Raman spectroscopy provides lateral resolution equal to the diffraction limit, therefore it is able to distinguish local changes of vanadium, or vanadium oxide stoichiometries. Moreover, it is readily available in the laboratory at Institute of Physical Eengineering, Faculty of Mechanical Engineering, Brno University of Technology (IPE FME BUT), where we conducted local oxidation experiments. Raman fingerprints of vanadium oxides are a well-known characteristic. A thorough review [34] served as inspiration for the possible outcomes we could obtain during our work. For the scope of this thesis, the understanding of several Raman fingerprints of vanadium phases was crucial.

Vanadium does not exhibit inelastic Raman shift, as it is a metal without vibrational modes suitable for Raman scattering, unless impurities are present, so we can easily distinguish between any modifications if we use a vanadium sample. The sample may inherently oxidize, we have however tried to minimalize this effect by modifying and characterizing vanadium-based samples as soon as they were fabricated.

The crucial vanadium oxides for our studies have proven (see Chapter 3) to be VO_2 and V_2O_5. VO_2 is a phase-change material [39] that transitions from insulator to metal once certain external stimuli [40] are applied (heat, electrical gating etc.). While the origin of its peculiar behaviour is debated [41], with either Mott insulator [42] or Peierls distorsion [43] the possible answers, the consequences of the phase-change are well known.

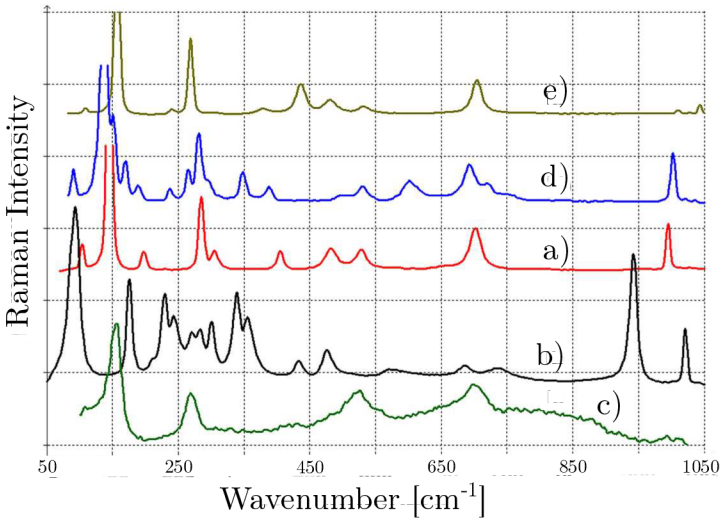

Fig. 1.7: Raman spectra of various V_2O_5 phases adapted from [34].

Aside from VO_2 changing its electronic structure, it also changes its crystalline form [44], going from a monoclinic (M1) phase to a rutile phase. Both of these phases can be detected using Raman spectroscopy (see **Fig.** 1.6). In [37] it was shown that when a V_2O_5 starting layer is used, one may obtain a slightly modified monoclinic VO_2 (B) phase with different lattice parameters. Such a monoclinic phase has its Raman fingerprint shown in **Fig.** 1.6 c). Another possible VO_2 polymorph can be obtained when hydrothermal reactions are employed during fabrication process [38]. This polymorph adopts a tetragonal structure, with its phase change temperature shifted to 162 °C. Its Raman fingerprints were measured at 30 °C **Fig.** 1.6 d) and 220 °C (see **Fig.** 1.6 e). Another vanadium oxide we have worked within this thesis is V_2O_5. V_2O_5 is another phase-change material. It also exhibits several possible crystalline structures. The most common being α-V_2O_5. α-V_2O_5

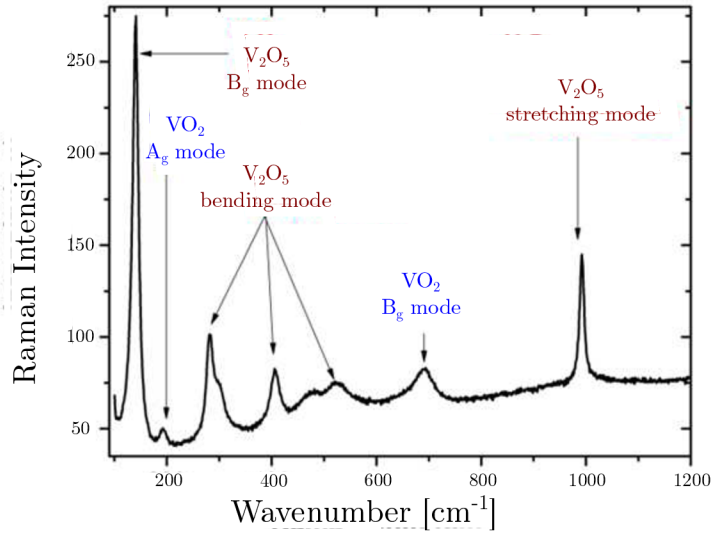

Fig. 1.8: Raman fingerprint of VO_2 particles. Adapted from [45].

has an orthorhombic crystal structure and has 21 Raman-active modes (see **Fig.** 1.7). If high pressure and high temperature are applied to α-V_2O_5 it will compress to a monoclinic crystal structure β-V_2O_5. Further compression leads to δ-V_2O_5 another monoclinic phase with slightly different lattice parameters. By removing metallic species from V_2O_5 bronzes we will obtain γ-V_2O_5, which has an orthorhombic structure with a different symmetry group compared to α-V_2O_5. Finally, an structurally undetermined phase of ε-V_2O_5 has been studied, with its Raman spectra being similar to α-V_2O_5 and γ-V_2O_5.

Unless optimal sample fabrication parameters are found, it is common to obtain several oxidation states within one sample. Raman spectroscopy can be used to detect several stoichiometries present within our sample, if we characterize it correctly. To ensure correct characterization, peak (corresponding to molecular vibrational mode) location and intensity plays a crucial role. In [45] VO_2 (B) particles prepared by microwave irradiation method were shown to contain traces of V_2O_5. This was confirmed by both Raman spectroscopy and XRD. The resulting Raman fingerprint contained two VO_2 vibrational modes, firstly, at $200\,\mathrm{cm}^{-1}$ a A_g (a mode with symmetry in inversion operation) and at $670\,\mathrm{cm}^{-1}$ a B_g (another mode with symmetry in inversion operation with different transformation properties in other symmetry operations, such as rotation). As for the V_2O_5 trace presence, five Raman peaks were shown. At $147\,\mathrm{cm}^{-1}$ a V_2O_5 B_g mode, three V-O bending modes at $310\,\mathrm{cm}^{-1}$, $404\,\mathrm{cm}^{-1}$, and $507\,\mathrm{cm}^{-1}$, lastly a vanadyl bond stretching mode at $992\,\mathrm{cm}^{-1}$.

2 NOVEL LOCAL OXIDATION METHOD WITHIN SEM CHAMBER

To locally oxidize vanadium-based thin films, a new method has been employed within the vacuum chamber of a scanning electron microscope (SEM) (see **Fig.** 2.1). The core parameters of each oxidation scheme, energy added to the sample and O_2 gas flow, were both addressed by applying hollow optical fibers. To manipulate these fibers during experiments conducted within the SEM vacuum chamber, we utilized a LiteScope AFM module and a Vacuum fiber micromanipulator (VFM described in [46]). We have employed various local oxidation setup combinations, with the crucial principles of local oxygen atmosphere and sufficient energy always in mind. We will now describe the two fundamental local oxidation variants as well as the characteristics of key methodological aspects, namely gas flow through a narrow capillary and hollow optical fibers used within this diploma thesis.

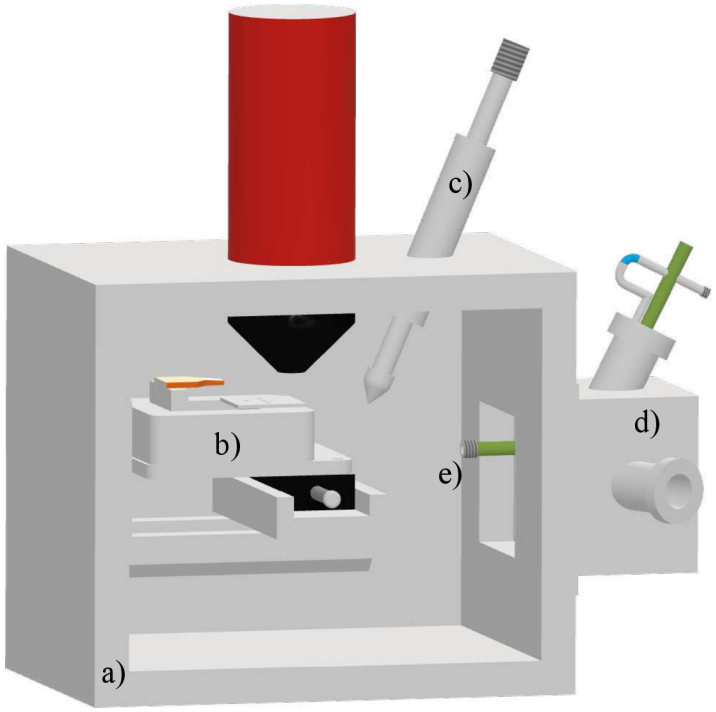

Fig. 2.1: Model of local oxidation system within a) SEM Vega used in this diploma thesis. The vacuum chamber accomodates: b) LiteScope AFM-in-SEM module, c)VFM d) multifunctional gas injection system with e) vacuum tight tubing coming into the chamber. The gas injection system can be

2.1 Capillary Gas Flow Dynamics

One of the crucial parts of this diploma thesis was understanding of gas flow through a thin capillary. This phenomenon has been studied throughout history, with ground-breaking work published by Danish physicist Martin Knudsen [47]. Knudsen first formulated the importance of ratio between mean free path and the character length of the system, which determines the nature of flow inside the system. Based on this ratio, often referred to as the Knudsen number Kn, we distinguish four gas flow regimes:

- *Continuum flow* (Kn $<$ 0.01). In continuum flow regime, the mean free path of particles is much smaller than the character length of the system. The gas behaves as a continuous medium as per frequent particle collisions. Continuum flow can be described by the Navier-Stokes equations [48].
- *Slip flow* (0.01 $<$ Kn $<$ 0.1). In slip flow regime, the mean free path of particles is comparable to the character length of the system. The gas still holds its continuum form to some extent, with noticeable slip velocity at the gas-solid interface. This regime follows the Navier-Stokes equations with a velocity boundary condition [49].
- *Transitional flow* (0.1 $<$ Kn $<$ 10). In transitional flow regime, the mean free path of particles is in the same order as the character length of the system. The gas behaviour is characterized by a mixture of molecular and continuum flow. This regime requires numerical calculations and specific models to accurately determine gas behaviour [50].
- Free molecular flow regime (Kn $>$ 10). In free molecular flow regime, the mean free path is greater than the character length of the system. The gas molecules behave independently from one another. This regime can be described using kinetic theory and follows molecular dynamics principles [51].

The first theoretical description of our problem, a thin capillary serving as a connector of two differently pressurized vessels, was performed by Ing. Jakub Zlámal, PhD. The model, in openFOAM software, consisted of a 10 cm long capillary of 1 µm diameter (see **Fig.** 2.2). This capillary has one end connected to a reservoir of oxygen molecules pressured to 1 bar (100 000 Pa), the other end is connected to a vacuum chamber with zero pressure. We have considered the capillary to be empty at first, with oxygen molecules flowing inside once the pressure difference is present. The results have shown that for the first 9.8 centimeters of our capillary, the oxygen flow will have a continuum flow progress. When the Knudsen number is taken into consideration, we can assume that narrower capillaries will need more time to permeate oxygen molecules through. This time dependance will be studied experimentally in the following sections. The following capillary region behaves as the transitional gas flow, therefore for theoretical description of gas flow in this region we would need more additional information about our fiber. However, gas flow in the final 4 mm of the capillary is in the molecular regime, so once the oxygen molecules successfully permeate through the capillary, we can describe the gas flowing to the sample surface using Monte Carlo simulations in Python.

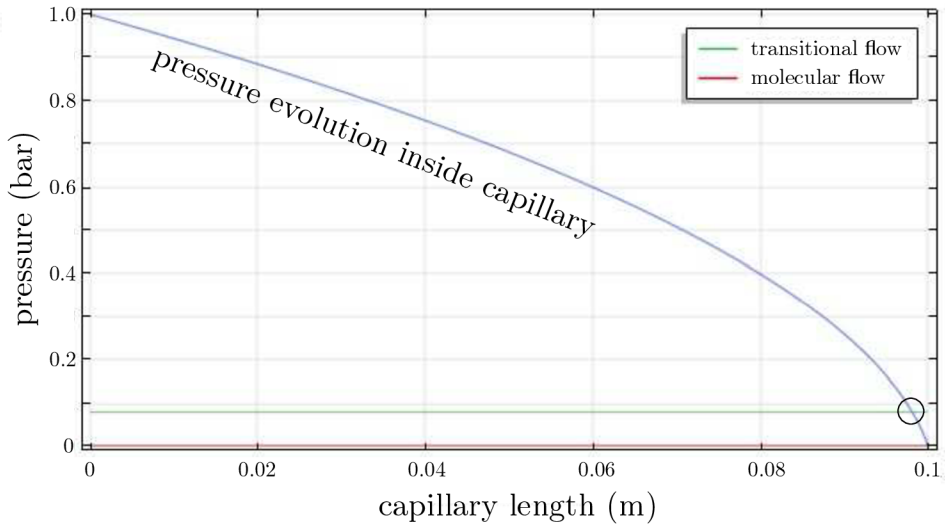

Fig. 2.2: Theoretical evolution of pressure inside a 1 µm 1 µm thin capillary. The model predicts transitional flow in the last 2 mm (where the blue pressure evolution inside the capillary intersects with the green curve representing transitional flow condition) and molecular flow at the very end (where the blue pressure evolution inside the capillary intersects with the red curve representing molecular flow condition) for 1 bar pressure difference. Work done by Ing. Jakub Zlámal, PhD. in openFOAM software.

In a simplified yet descriptive approach of solving gas flow through the end of a capillary, we have considered the following model (see **Fig.** 2.3) to determine the region of thin film exposed to oxygen molecules for various surface-capillary distances (see **Fig.** 2.4). A 1 µm in diameter tube (capillary) contains oxygen molecules. These oxygen molecules are adsorbed on the inner surface of the capillary and can desorb into the free space. The direction of desorption is proportional to $\cos\Theta$, where Θ is the angle between direction of

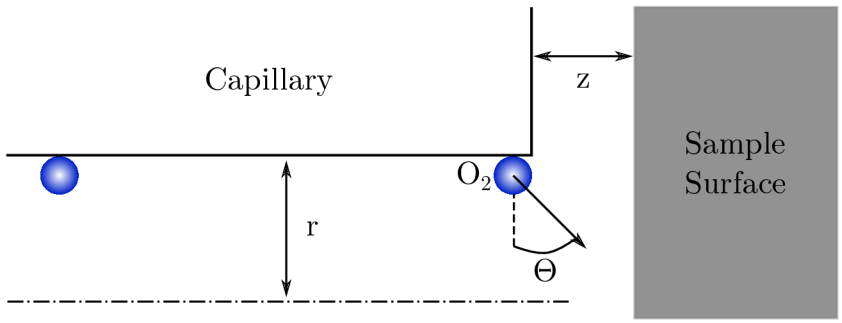

Fig. 2.3: Oxygen gas flow through capillary in molecular regime. A thin capillary of radius r is within z distance from sample surface. Oxygen molecules of Knudsen number $\mathrm{Kn} > 10$ desorb from the capillary surface. The rate of desorption follows the $\cos\Theta$ law, with the most probable direction being perpendicular to the capillary surface. By adjusting the distance between the capillary and the sample, we can change the surface density of oxygen molecules adsorbed on the surface.

travel and vector normal to the capillary surface [52]. Here we assumed the particle flow inside the capillary to be molecular, as per results from openFOAM software simulations. To describe the behaviour of such a model, Monte Carlo simulation have been conducted in python where particles were assigned random values of desorption angles. We then monitored the number of particles impinging on a planar surface in several z distances, with surface particle density and overall spot size taken into consideration. This problem is rotationally symmetrical, so one-dimensional calculation sufficed for the system description.

In near-contact mode ($z \to 0$), approximately 80 % of the incoming oxygen particles fall within a circle with a diameter of 1 µm, with a saddle in the axis of the capillary (see **Fig.** 2.4). This saddle deepens the further as we increase the z distance, along with the particle coverage radius increase. If we take into consideration a finite number of molecules we are able to supply from the capillary (in our simulations, we traced 10^6 particles), we run into a theoretical utility distance limit at $z_{\text{lim}} \propto 60$ µm. Here, the gas particle coverage radius (that is an area where 80% of incident particles adsorb on sample surface) is 58 µm with nearly uniform coverage, below 0.2 % of incident atoms per µm^2. If we increase the size of the capillary, the results seem scaleable, with optimal gas distribution being

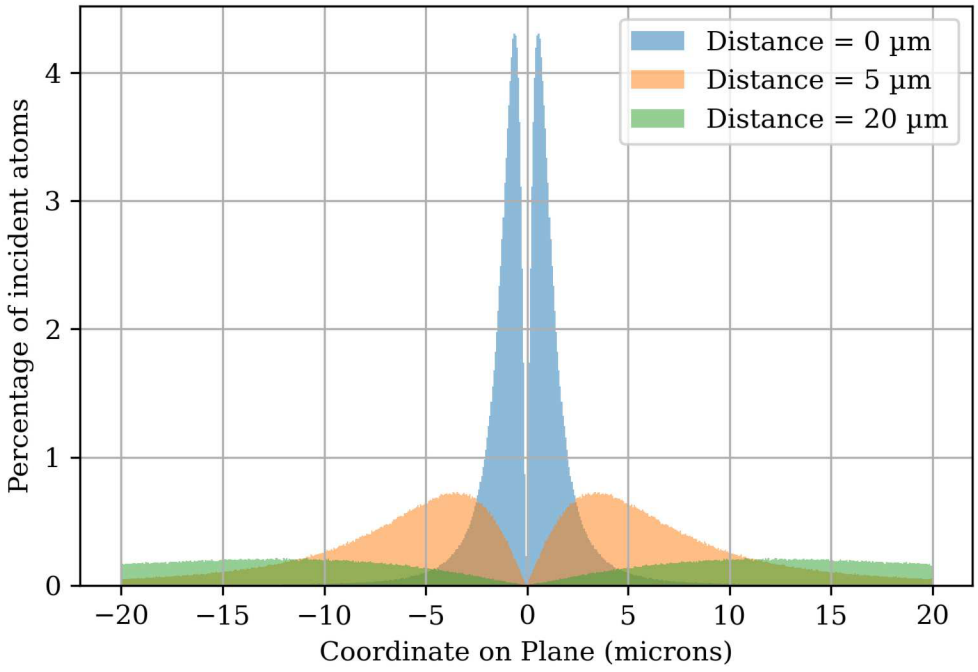

Fig. 2.4: Distribution of incident oxygen molecules coming from a 1 µm thin capillary. The distribution trend is similar for all sample-capillary z distances with a saddle directly below the capillary axis. The oxygen coverage per unit area changes dramatically over relatively short z distances, with significant differences visible even at 4 µm z distance change.

again in contact mode. We must, however, consider additional benefits of having a larger capillary in the overall gas flow dynamics. More oxygen atoms will reach the end of the capillary when its diameter enlarges and they will do so faster than when a smaller diameter capillary is used. Our simplified model therefore provides useful insight when sample distance is considered, for experimental results, theory alone will not suffice and further characterization will be required.

Based on our model following the cosine law of desorption, another phenomenon should appear once the capillary is within close proximity to the sample surface (due to the system's character length being changed). Since the capillary is encapsuled by solid glass with the cladding diameter significantly larger than the capillary diameter, we can expect a similar series of oxygen molecules adsorbing/desorbing events between the face of the hollow fiber and the sample surface. Due to the capillary and fiber face diameter mismatch, we can predict a significant confinement of oxygen molecules to the face of the capillary. This phenomenon of local atmospheric increase is greatly in favor of our newly local oxidation endeavor. Our model is however not able to show this effect, since the frequent collisions between the oxygen molecules, that occur due to the fiber face and sample surface confinement, cause the gas flow to no longer be molecular. If we use such a fiber as an AFM probe, this phenomenon should be observable during AFM measurements in the change of resonant frequency of such an AFM probe. If we get close enough to the sample with a planar probe, the change of density in the local atmosphere should shift the resonant frequency as well as dampen the amplitude of oscillations. A somewhat similar situation can be observed when probe quality factor measurements are conducted at different global pressures.

2.2 Hollow optical fibers

For the purposes of locally oxidizing vanadium-based samples we have utilized two photonic crystal fibers (PCFs), each with their own limitations and advantages. PCF is a waveguide with a large number of narrow (usually in the range of a few µm) capillaries. Within the PCF family, the core can be either solid or hollow. Solid-core PCFs guide light similarly to traditional optical fibers, where, an area of high index of refraction (core) is surrounded by an area of lower effective refractive index (cladding). This ensures total internal reflection can take place at the core/cladding junction. Firstly, we have used a LMA-5 fiber made by NKT Photonics [53] (see **Fig.** 2.5a). This fiber utilizes an array of holes structured into a so called large mode area (LMA), a principle mostly used to prevent nonlinear effects and material damage. The LMA-5 fiber has the smallest solid core from the LMA fiber family, coming at a 5 µm diameter, which was suitable for keeping areas of local oxidation as defined as possible. Aditional advantage of the LMA-5 fiber was easier light coupling given by its higher numerical aperture. We were able to efficiently transfer up to 80% power from a standard single mode fiber to the LMA-5. While the power output of the LMA-5 fiber is near ideal for our purposes, its gas transfer functionality is somewhat questionable. The fiber has its core surrounded by numerous holes. However the holes (capillaries) are just 1 µm in diameter. When these dimensions are taken into consideration with the knowledge of gas flow through narrow capillaries discussed in Section 2.1, the conclusions are as follows:

- *Pressure difference*: We have to exert a higher pressure difference at the ends of the fiber to *push* oxygen through as per the predicted gas flow complexities.
- *Time*: We can also expect for oxygen permeation to take more time than for fibers with larger capillaries. Similar conclusion can be made for longer fibers; the longer the fiber, the more time will be required for oxygen permeation.
- *Capillary-sample z distance*: While the molecular flow condition may be met at the very end of the capillary, the capillary distance from sample will play a crucial role as we can expect a significant decrease of gas coverage as we move the sample further. Here we are limited by the precision of fiber manipulator movements.

The LMA-5 fiber therefore needed further characterization mainly for its gas injection capabilities. These theoretical limitations were experimentally explored and are discussed in the Section 2.2.2.

The second fiber used within this diploma thesis was the PCF PM-1550-01 from Thorlabs [54] (see **Fig.** 2.5 b), a polarization maintaining (PM) fiber. PM fibers can maintain linear polarization of incident light when the light is coupled properly into the fiber. PM fibers work on the principle of intentional birefringence inside the fiber. The polarization states of incoming light induce various modes within the fiber and a PM fiber has features that create modes of opposite phase for any light polarization other than the nominal. The created modes of opposite phases cause a destructive interference between them and the fiber maintains only one polarization of light. In the PM-1550-01, the birefringence

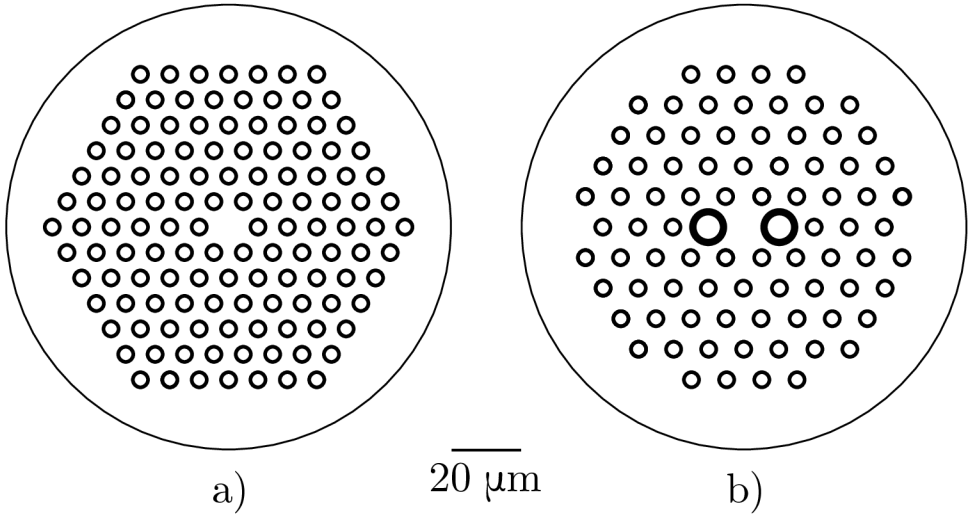

Fig. 2.5: Selected fiber cross sections. a) LMA-5 fiber from [53] with a large array of 1 µm holes and a central 5 µm waveguiding core. b) PM-1550-01 fiber from [54] with two 5 µm holes near waveguiding core.

is ensured by two 5 µm holes, symmetrically separated by the solid fiber core (a so-called panda cross-section). Along with the two 5 µm holes the face of the PM-1550-01 has a photonic crystal structure, so numerous other 1 µm holes can help inject gas into our regions of interest. The core diameter is again 5 µm allowing for adequate definition of local oxidation. The main disadvantage when using the PM-1550-01 as opposed to the LMA-5 for local oxidation was paradoxically the PM property. We used a partially polarized source of light in the form of a CW $1,5$ W green laser $\lambda = 532$ nm (described in [55]), so coupling sufficient power from one fiber to the PM-1550-01 PCF posed a challenge.

2.2.1 Gas flow and light coupling in multifunctional gas injection system

For coupling gas and light into the vacuum chamber of SEM via PCF we had our path paved by prior work conducted by Ing. Ondrej Černek. He solved the problem of bringing pressurized gas into the SEM chamber of VEGA Tescan by modifying the chamber door [56]. Since then we have changed systems, to a newer version of VEGA SEM, so construction work needed to be done. Firstly, a reduction has been made to accomodate the custom chamber door into a side plug in SEM microscope. This meant we could use the chamber door as they were intended without compromising our new multifunctional gas injection system with constant reassembly. The gas was brought into the SEM chamber by vacuum tight tubing connected to a flange using vacuum compatible fittings. Before our work, the multifunctional gas injection system (vacuum-tight tubing) had to consist of several Swagelok parts, otherwise it would not be sufficiently long (as the new SEM system chamber is larger).

Due to numerous vacuum problems (when a pressure difference of several orders of magnitude is present within a tube inside the chamber of an electron microscope, any slight leaks mean the SEM imaging is non operational). We have therefore opted to weld a single stainless steel tube onto the vacuum flange. At the SEM end of our multifunctional gas injection system, a tight fitting is present, with a custom made teflon seal used to block gas coming into the chamber, greatly reducing the potential leaks. Depending on our selected experimental setup (see Sections 2.3 and 2.4), we can then couple both gas and light into the hollow fiber or just gas. The former approach requires fixing a ferrule over both fibers and connecting them using a copper sleeve (see **Fig.** 2.6), while the latter only requires a teflon fitting to ensure vacuum tightness of SEM chamber. By moving the

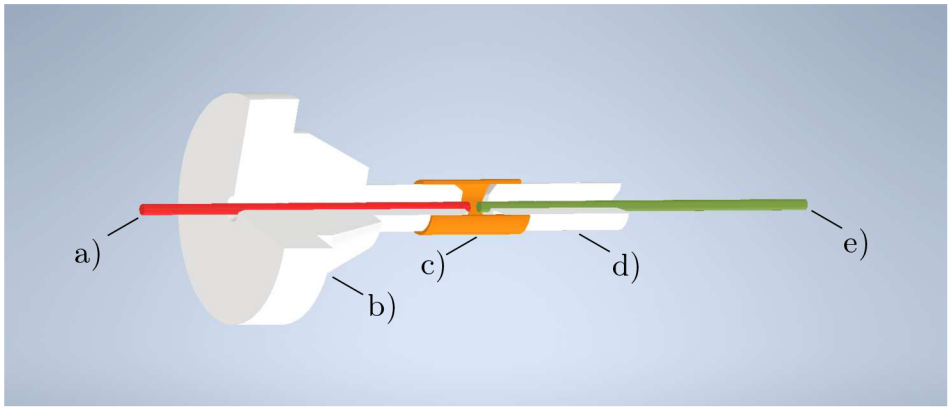

Fig. 2.6: Fiber coupling mechanism used within the multifunctional gas injection system. a) PCF fiber inside a custom made teflon fitting b) is connected via a 2 cm long concentric sleeve c) to a single mode fiber e) that is fixed inside a single mode ferrule d). By moving the ferrule closer to the PCF we can increment laser light power output, with up to 80 % coupling efficiency. Both fibers must have planar faces to ensure maximal efficiency.

ferrules inside the sleeve, we can maximize laser light power output. Any crashes between the fibers significantly reduce the laser light coupling efficiency, it is therefore beneficial to fix the fibers inside the ferrules once optimal. Coupling just gas into the capillary is more straightforward, only tightening of the teflon fitting is needed to ensure that the only real source of oxygen is the other end of our hollow fiber (that can glued to a quartz tuning fork, forming an AFM probe). As discussed briefly in the paragraph 2.2, the choice of fiber is not trivial and gas flow characterization needed to take place to better define our novel local oxidation method.

2.2.2 Gas flow characterization

To reassure that gas flow through our hollow optical fibers was indeed possible, we have first employed a trivial test. We have simply connected one end of the fiber to the oxygen source and submerged the other end into water. For PM-1550-01 fiber bubbles at the end of the fiber have formed instantaneously and kept blowing into water at a steady rate. For the LMA-5 fiber, after the oxygen was allowed to flow in our multifunctional

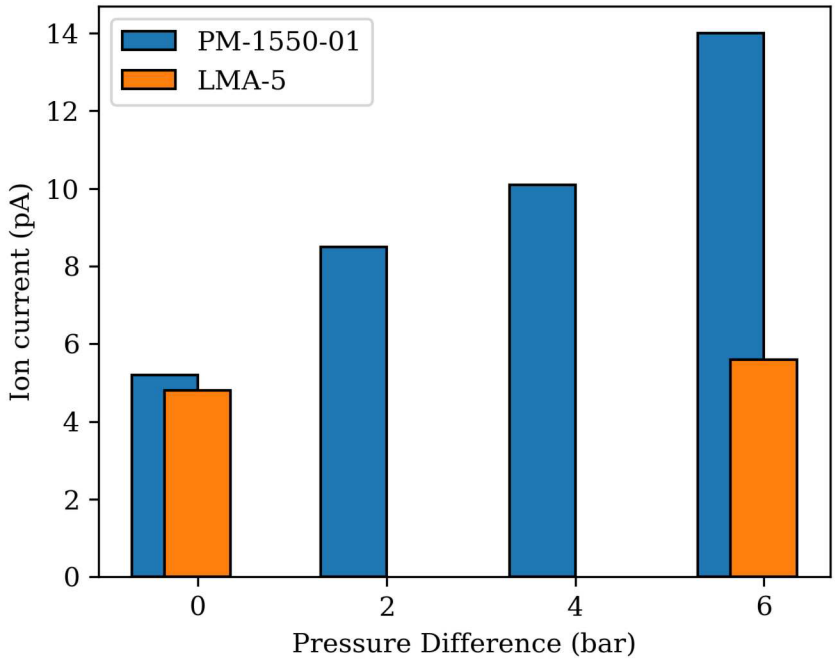

Fig. 2.7: Residual gas analysis (RGA) of O_2 particles coming into a vacuum chamber from different PCFs at various pressure differences. For the PM-1550-01 the change in current happened over mere seconds as we incremented pressure. We had to wait over 24 hours for the current of O_2 molecules to change while using LMA-5 fiber. No change in pressure was measured inside the vacuum chamber. No other element showed a considerable increase in ion current once pressure difference was established.

gas injection system, gas bubbles began forming after a longer period of time (minutes). This has served us as a test of whether we are even able to bring any type of gas into the fiber tip vicinity, we were still lacking concrete evidence as to what gas was flowing through the fibers. We decided to test this in the following manner: We would pump the multifunctional gas injection system through the microscope overnight and measure RGA using a mass spectrometer (Quadera Mass Spectrometer model made by Pfeiffer Vacuum). Once the system was of sufficient vacuum, we would continuously measure user defined masses of atoms (see **Fig.** 2.7). Only then would we allow oxygen to flow through the fiber into the vicinity of the mass spectrometer (by placing the end of the fiber in front of the mass spectrometer RGA entrance).

For the PM-1550-01, the gas flow results were promising. Seconds after opening our pressurized multifunctional gas injection system, the mass spectometer showed an increase of oxygen molecules. This happened without vacuum breaking inside the SEM vacuum chamber, so only the hollow fiber could have been a source of gas. Combined with the quick response time, mere seconds before gas permeated through the fiber, the PM-1550-01 was a suitable choice for our following local oxidation experiments.

For the LMA-5, the same experiment was done. However, only after approximately 24 hours since the gas valve was opened, oxygen started flowing through the fiber. We have expected a difference due to the capillary dimensions (see **Fig.** 2.5), however this has rendered the utility of the LMA-5 fiber very limited. Any local oxidation using the LMA-5 fiber must be prepared 24 hours before the experiment. Also, the amount of oxygen gas flowing through was roughly half of the value given by the PM-1550-01 fiber at the exact pressure difference. Waiting such a long time for a significantly smaller amount of oxygen is not outweighed by the simplified coupling. Once these gas injection experimental results were clear, we have only used the PM-1550-01 fiber in the following experiments.

Since the response of the PM-1550-01 fiber was so fast, we have tested how the flow behaviour changes when we increase the pressure difference. Similarly to the test above, we have left the vacuum system on overnight to ensure optimal measurement using the mass spectrometer. When the valve first opened at $p_{\text{in}} = 2\,\text{bar}$, we have again seen a near instant rise of oxygen species ion current. The amount of oxygen in the vacuum chamber always settled at a constant value. Then we increased the pressure difference to 4 bar and 6 bar. As is evident from the graph **Fig.** 2.7, we were able to successfully increment the amount of oxygen coming into the SEM vacuum chamber with both the PM-1550-01 and LMA-5 fibers, with the former shown as the better choice due to the reaction time and amount of gas transferred into the system at a given pressure difference. We have therefore achieved control over a pivotal parameter in our local oxidation processes, ensuring quantitative manipulation of oxygen levels during our experiments.

2.3 Single Fiber Manipulator Method

We started with the mechanically simplest variation of local oxidation using hollow optical fibers. Pressurized O_2 gas was led inside the SEM chamber using our developed multifunctional gas injection system described in Section 2.2.1. Inside the tubing a plain single mode fiber coupled to the 1.5 W green laser is fixed in a ferrule. Between the tubing, and the vacuum chamber a custom made teflon fitting with another ferrule is placed, with a hollow PCF placed inside the fitting. The two ferrules are then connected with a concentric sleeve, ensuring high coupling ratio (up to 70 % laser light power can be transferred from one fiber to the other). The teflon fitting is then tightened by a cap causing only the hollow fiber capillaries to transfer gas into the SEM chamber, while maintaining high vacuum needed for imaging in an electron microscope. The other end of the hollow fiber is then glued onto a quartz tuning fork, that can be precisely manipulated using only the LiteScope AFM module for SEM [57], hence single fiber manipulator method.

The single fiber manipulator method (shown in **Fig.** 2.8) allowed for $\approx 25\,\%$ of total laser light power to be coupled to the AFM probe along with oxygen flowing in the probe vicinity. To achieve optimal power transfer, the face of the hollow fiber was planar. This necessity rendered the lateral resolution of such AFM probes to be insufficient and, while the probe was able to successfully approach the sample surface, AFM topography measurements were not conducted. Also, due to high pressures needed to push oxygen through the fiber capillaries, to decrease the oxygen flow proved challenging. Once the gas pushed through the capillaries, a substantial gas reservoir was formed inside the tubing of our multifunctional gas injection system. Stopping gas flow was impossible without

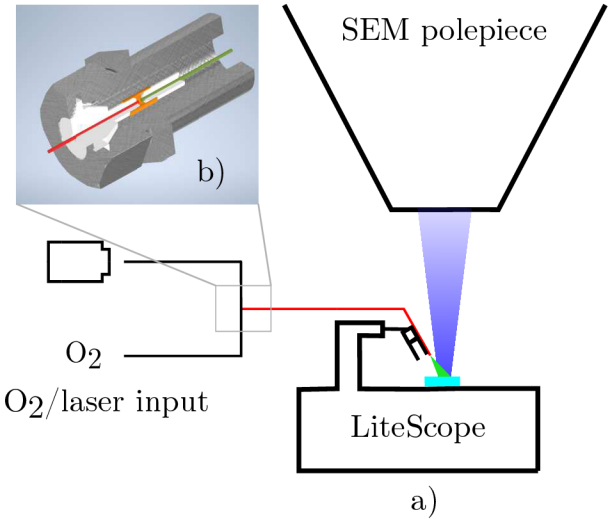

Fig. 2.8: Schematic of a single fiber manipulator setup. Gas and laser light is coupled by utilizing multifunctional gas injection system, within it a compression fitting deforms the teflon fitting (see Section 2.2.1) so only the PCF can transport gas particles between the injection system tubing b) and SEM vacuum chamber a). The PCF is manipulated using LiteScope AFM module enabling precise movements with *in situ* SEM imaging.

venting the entire SEM chamber along with the gas tubing. The ability to stop/start gas flow was necessary for etching alignment marks into the sample. For this purpose, we want to change the sample surface properties enough to be seen in conventional optical microscopy without necessarily modifying its stoichiometry and interfering with the following oxidation experiment in an undefined way.

In this diploma thesis, we have revisited our single fiber manipulator method with newly acquired knowledge about our hollow fibers gas injection properties (see Section 2.2.2) as well as the distribution of oxygen particles (see **Fig.** 2.4). We have also seen (as will be shown in Section 3.2.3) that when we successfully oxidize a region on the sample, the site may be visible in optical microscopes. This occurred even at low laser powers, as will be shown in the chapter 3. The necessity for macro alignment marks was therefore negligeable, as the single fiber manipulator method proved successful in the end (see Section 3.2.3).

2.4 Twin Fiber Manipulator Method

Here we utilized another fiber manipulator, along with LiteScope, in the form of the vacuum (fiber) micromanipulator (VFM) [46]. VFM is best suited to bring a single fiber inside the SEM, we could therefore split the crucial oxidation principles into two. VFM served as a source of light. Gas intake was resolved in a similar manner to the Section 2.2.1. With no additional fiber coupling needed inside the vacuum tubes of the multifunctional gas injection system, a simple teflon fitting sufficed to keep gas flow only within the vicinity of the AFM probe. Thus maintaining high-enough vacuum to enable imaging inside the SEM for local oxidation experiments.

In our twin fiber manipulator method, the gas was separated from the light source, meaning we could locally modify the sample surface to form alignment marks. Since the

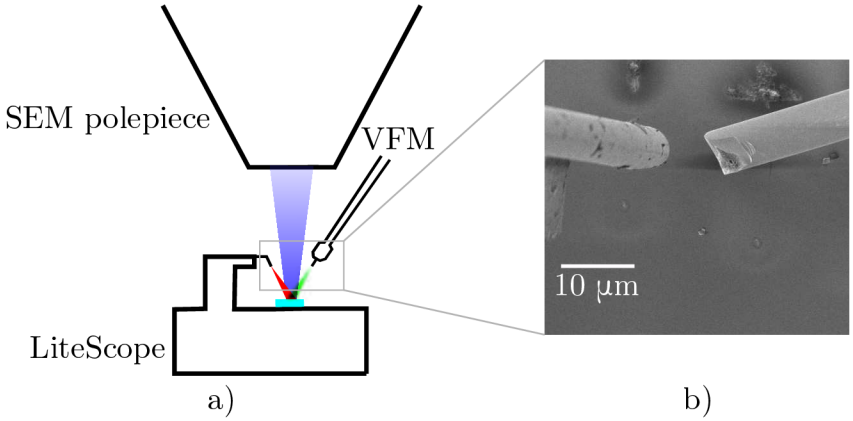

Fig. 2.9: Schematic of a twin fiber manipulator setup a). A hollow AFM probe with a sharp tip can (left fiber of detail b) is brought within 10 µm from a solid optical fiber (right fiber of detail a), allowing for local oxidation of sample surface.

custom AFM probe no longer needed to be planar to bring the laser light in a defined manner, a tip was made on top of the hollow fiber. This elevated the LiteScope function from a fiber manipulator to its full potential and enabled AFM measurments to take place during/after local oxidation experiments. In this way, we have found two possible approaches based on the twin fiber configurations. In **Fig.** 2.10 a), the fiber from VFM (light source) is within microns from the surface, and the AFM probe (gas inlet) is tens of microns away, providing a local O_2 atmosphere. The minimal surface–VFM fiber distance is done using macro motors of the SEM stage holder. The macro motors are not as precise as the piezo motors of LiteScope AFM module, so we will never achieve the same proximity and reliability with VFM. Another slight disadvantage is the fact that each LiteScope AFM probe–VFM fiber configuration will have a different angle between the fiber face and sample surface. Due to the surface–probe distance, topography measurements had to be done after each local oxidation experiment. In **Fig.** 2.10 b, the fiber from LiteScope AFM probe is in contact mode with the sample surface and the VFM fiber shines underneath the tip. This fiber configuration was difficult to set up but showed new properties, briefly discussed in Chapter 3. We deposited a reflective metallic layer on the probe, thus locally enhancing light reflected from the sample by the tip, similarly to tip enhanced Raman spectroscopy [58] principle. This allowed for *in situ* AFM topography measurement of local oxidation to take place.

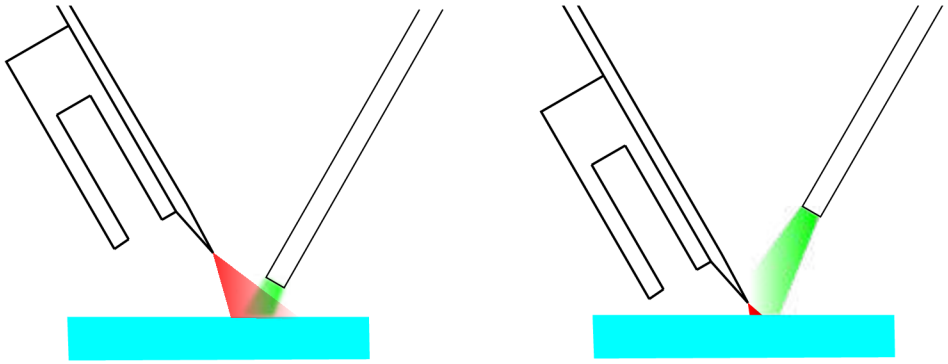

Fig. 2.10: Possible twin manipulator configuration schemes. a) VFM fiber is in contact with the sample surface and an AFM probe (PCF fiber glued to quartz tuning fork) provides O_2 atmosphere from a variable distance. b) AFM probe in contact mode measuring topography, with VFM fiber further away for possible local O_2 atmosphere (with laser light reflecting from the AFM probe tip).

3 RESULTS AND DISCUSSION

In this section we will present the obtained experimental results, as well as some other practical insights into our local oxidation method developed in the frame of this diploma thesis. We begin by discussing selected substrates, followed by sputtering of vanadium-based thin films. Later, we present results achieved by various local oxidation schemes along with characterization of sample topography and optical properties.

3.1 Sputtered vanadium-based thin films

We have used the IBAD apparatus (described in the Section 1.1) for thin film fabrication. We have kept the flow of Ar atoms at the value of 7 sccm. This value provided optimal amount of primary ions and kept the vacuum inside the deposition chamber at $5 \cdot 10^{-4}$ mbar. When fabricating V_xO_y thin films, we used the secondary ion source to bring O_2 atoms into the deposition chamber. The flow of O_2 atoms was kept relatively low, to maintain high enough vacuum, at 3 sccm. Experiments with both the primary and secondary ion sources active were operating at vacuum level $6.5 \cdot 10^{-4}$ mbar. As substrates, both fused silica and silicon were used due to their heat conduction properties. Thermal conductivity of fused silica at room temperature is one of the lowest for solid materials, reaching a value of $1.38\,\mathrm{Wm^{-1}K^{-1}}$ [59]. It is therefore safe to assume any heat we induce during local oxidation will remain inside the thin vanadium layer for a longer period of time, increasing the potential for local modifications. On the other hand, the thermal conductivity of silicon substrates at room temperature reaches $139.4\,\mathrm{Wm^{-1}K^{-1}}$ [60].

Prior to deposition, substrates were cleaned using ultrasonic bath in acetone and IPA. The vanadium target was sputtered for 15 minutes in advance, to ensure a clean surface of the target. Thin vanadium films prepared by IBAD technique had a typically silver, metallic color and were about 100 nm (measured by AFM) thin with deposition rate $0.8\,\mathrm{Å s^{-1}}$. The V_xO_y had a slightly blue tint with the same layer thickness.

3.2 Local oxidation of vanadium-based thin films

One of the objectives of this diploma thesis was to develop, describe, and effectively utilize a newly designed local oxidation setup. Since this method was never used before, we have tested and developed quality of life improvements as the experimental results came. In this section, we will focus on the principal experimental knowledge of each methodological variant. We will also present characterization results and improvements made to the setup based on our prior studies.

3.2.1 Single Fiber Local Oxidation in SEM

Starting with the single fiber manipulator method, as described in Section 2.3, we began our experiments using LMA-5 fiber (see **Fig.** 2.5) for local O_2 gas atmosphere and local heating using laser light. We cut the face of the probe planar by a ruby knife, the tip of the probe was sharp enough to approach sample surface without problems and planar enough to keep a well defined laser spot. We sharpened the fiber by using sandpaper (this method was invented by Ing. Z. Nováček, PhD.). We rotated the fiber and pressed it to the sandpaper (sand grain size 150 µm). Depending on the force, the formed tip sharpness changed, until we found a tip optimal for our use case. We have then coupled both O_2 gas and laser light into the AFM probe using the multifunctional gas injection system developed within the scope of this diploma thesis (see Section 2.2.1). With the LMA-5 fiber, we usually managed to couple 25 % of laser power into the tip of the probe (measured with a Thorlabs PM100D power meter). For each experiment, we measured this ratio and always took into cosideration just the power of light coming out of the

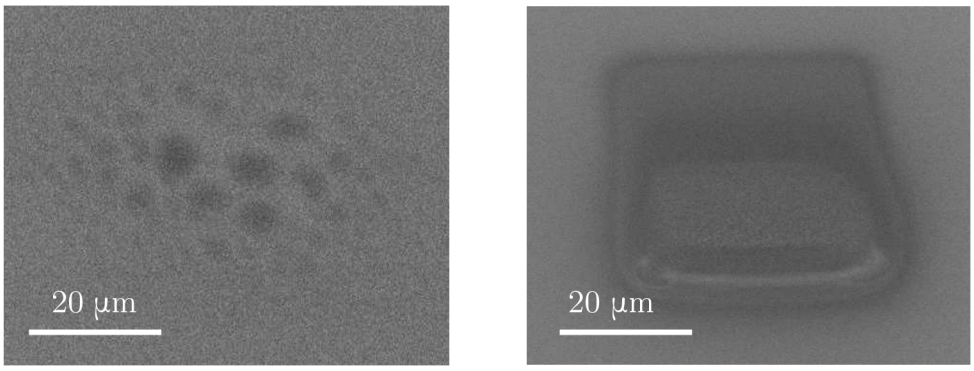

a) b)

Fig. 3.1: SEM images of dwell time testing for $P_{vis} = 50$ mW laser power. Both 40×40 µm^2 arrays were modified using the LMA-5 fiber with 6 bar pressure O_2 inlet. The scan was made out of a) 32 points per line (ppl) and b) 64 ppl. A clear difference in modified region is visible, lower dwell times cause the modification process to be distributed into singular areas; if we increase dwell time, the areas the individual grain influence each other and form a single modification site.

probe. We then waited 24 hours before the 6 bar pressure O_2 gas permeated through, as described in Section 2.1. The first samples we modified were V_xO_y, sputtered on fused silica substrates.

During the first local oxidation experiments, we used the piezo scanner of LiteScope AFM in SEM module to define our region of interest. We experimented with laser power needed to visibly modify the sample surface as well as the laser dwell time. The first visible results came at $P_{\text{vis}} = 50\,\text{mW}$ laser light output power. We have decided to characterize the array dwell time (see **Fig.** 3.1) by the number of points the probe took in each scan line (ppl). LiteScope AFM module allows only one probe scan speed, with a user-defined number of points forming each scan line (ppl). The amount of time spent on each point is the same for every number of ppl. Therefore, if we double the ppl, we double the array dwell time. For 32 ppl the resulting $40 \times 40\,\mu\text{m}^2$ arrays were made of singular oxidation spots (see **Fig.** 3.1a). For 64 ppl the same array size was modified in a more unified way, with the oxidation site given enough time to converge into a probably single island.

First fundamental problems arose with the sample characterization. The modified sites have not changed their oxidation state, rather, they were melted, ablated regions of our thin layers. This was shown in inconclusive Raman fingerprint characterization, where the modified areas proved to just reflect more light, rather than show new peaks corresponding to any known vanadium oxide stoichiometry. This in itself could just be an issue of not having the correct oxidation parameters, however, there was another problem. As a result of the thin layer evaporation vanadium-based debris started forming atop our probe (see **Fig.** 3.2). This vanadium debris systematically reduced the power of incident light reaching the oxidation site due to light scattering or absorption in the vanadium residue. We could see this effect take place when we tried repeating the same oxidation sites on one sample or when we were creating a longer macro mark for alignment purposes.

The modifications we could see by *in situ* imaging inside the SEM and after fabrication in optical microscope were not stoichiometrical changes of oxidation states, as Raman spectroscopy measurements shown. A decision has been made to use lower laser powers for oxidation, as we could not detect stoichiometrical changes using SEM, but first to form well defined alignment marks using high enough powers to be visible in optical microscope (for following optical characterization of local oxidation sites). We could then reference ourselves accordingly and navigate on our sample without the oxidation sites necessarily visible during characterization. Due to the necessity of often removing the vanadium debris, when using higher powers to evaporate the alignment marks, we have decided to use the twin fiber manipulator method as described in Section 2.4 on page 28.

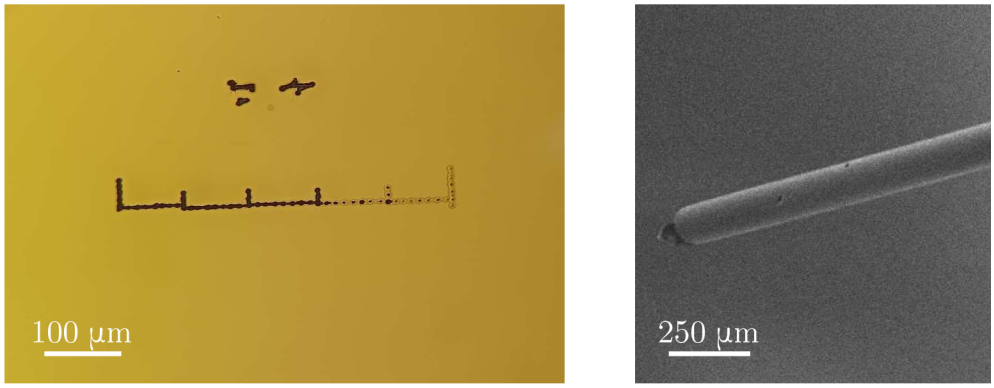

a) b)

Fig. 3.2: a) Modified sites contrast decrease during modification experiments. Due to thin layer evaporation by initially high laser power output, b) vanadium residue forms near the tip of optical fiber used. This residue causes light scattering on the tip and power output decrease.

3.2.2 Twin Fiber Local Oxidation in SEM

Following on the experimental challenges of the prior paragraphs we have began using two fiber manipulators in order to divide the local oxidation into two processes. We opted for a 100 nm thin vanadium film on fused silica, as we were sure of its absorption of green light (as opposed to the undefined absorption of V_xO_y thin films). We coupled light into an optical fiber inside the VFM described in Section 2.4. This meant we had one less light transfer, therefore we had double the maximum output power of laser light. We

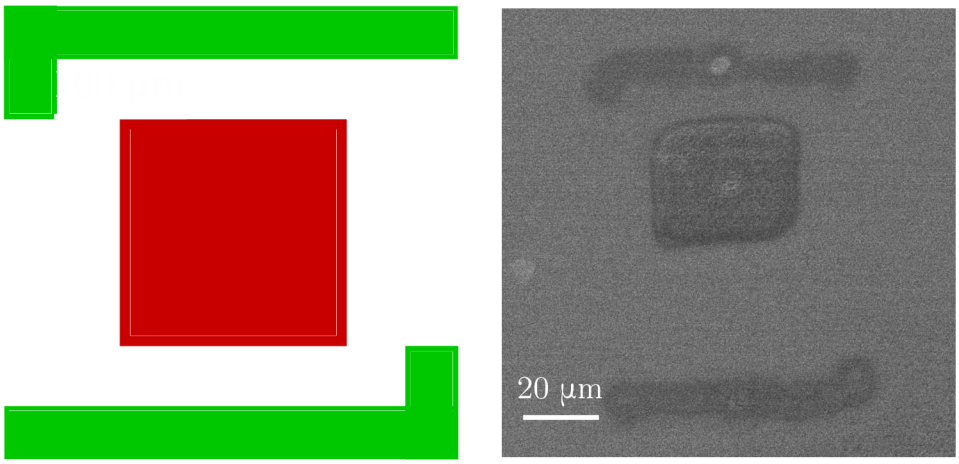

a) b)

Fig. 3.3: Alignment mark-scanned array configuration. a) Schematic drawing, and b) SEM image of used modification geometries. Firstly, "L" shapes are fabricated only using laser light and serve as alignment marks for future sample characterization. Secondly, square modifications are fabricated, using laser light and close proximity of gas injecting AFM probe.

fabricated a sharp tip on the end of a 10 cm long piece of PM-1550-01 fiber (**Fig.** 2.5 b) and coupled gas into it. As stated above, we divided the process into two steps. The first step was done solely by light coming from VFM fiber. We came into fiber-surface contact and ablated marks using 50 mW laser light power. We decided to draw two "L" shaped marks on the edges of a 80 µm field using the using the LiteScope piezo motors, see **Fig.** 3.3. This was done by programming the movement of the piezo scanner, enabled by overwriting the scan center offset. Controlled and reproducible marks were always created this way prior to the second step.

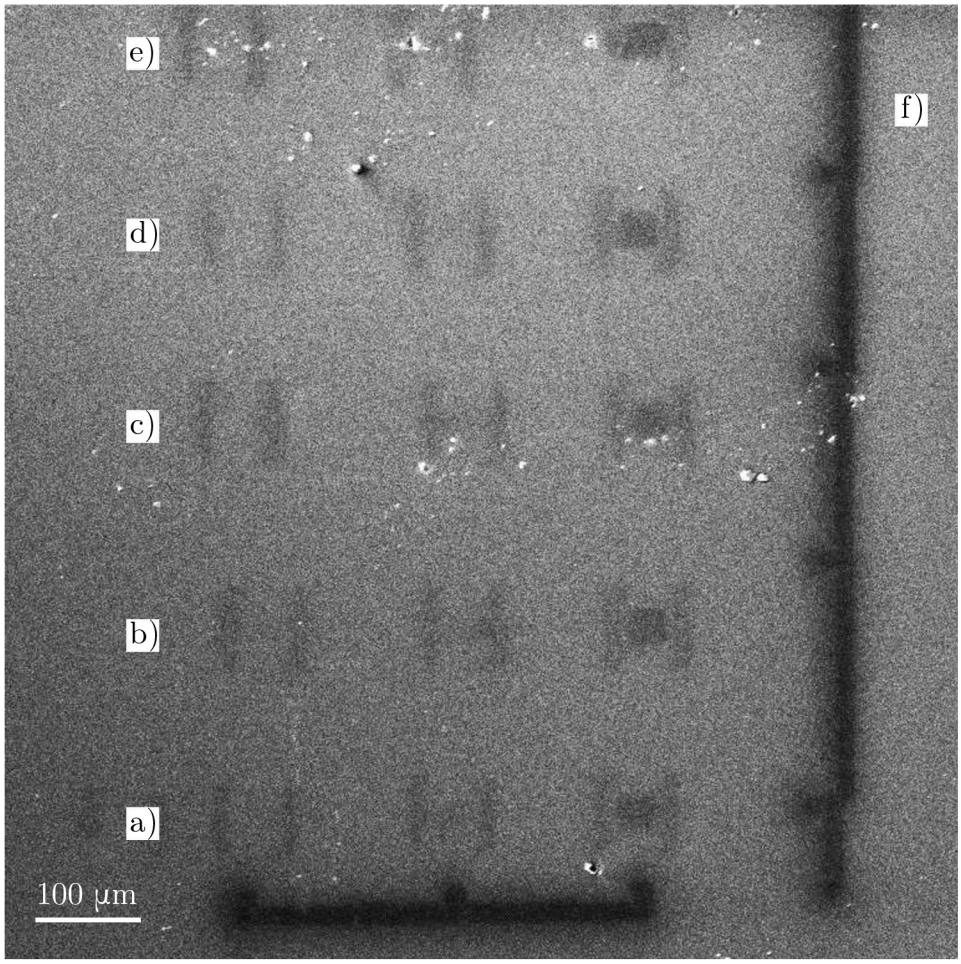

Fig. 3.4: SEM image of a vanadium thin film (on fused silica substrate) modified by three laser light powers. 20 mW (left column), 30 mW (middle column), 50 mW (right column). The probe (gas inlet) distance varies for each line, 200 µm for line a), 150 µm for line b), 100 µm for line c), 50 µm for line d) and 0 µm (probe in contact mode) for line e). Each array is encapsuled by ablated "L" shape alignment marks created without oxygen probe proximity using $P_{\text{vis}} = 75$ mW laser light power. f) The entire geometry is surrounded by macro marks in the form of scale bars, for better sample orientation outside the SEM. The scalebars were made last due to possible fiber contamination, as such, they were made using higher laser light powers starting at $P_{\text{max}} \propto 100$ mW (that had to be incremented due to vanadium residue forming on the fiber).

In the second step, we brought the hollow AFM probe close to the VFM fiber. By varying the configuration of the two fibers, namely the probe z distance from sample surface (we kept the fibers 5 µm in x axis and level in y), we searched for optimal local oxidation parameters. We kept alignment mark geometries similar to **Fig.** 3.4. The fiber in VFM remained in contact with the sample surface and by moving just the piezo stage we kept the marks and oxidation sites aligned for further characterization. To minimize the residue forming on the VFM fiber, a process of high power laser flashing was involved: Here, we moved the surface of the sample away from the fiber in just the z axis and used 500 mW power of laser light to evaporate any vanadium from the tip of the fiber. We then moved the sample surface back to into contact mode with the VFM fiber and carried on in our experiments. This high laser light power evaporation was done after every array was finished, increasing the lifetime of our fiber significantly. The effect of residual vanadium decreasing the laser light power was still slightly visible, we have therefore compensated the output power after each array by 2.5 mW. After every 4 fields, we have shortened the VFM fiber to refresh its spot size and laser light power output. Five probe-sample distances were tested, ranging from 200 µm to contact mode with 50 µm step. Having a sharp probe enabled measurement of topography.

We have therefore gained additional information about our sample properties. As expected, the first step of fabrication, the macro mark ablation created holes inside our thin vanadium layer (top of **Fig.** 3.6). The locally modified oxidation region proved to be growth sites of roughly 100 nm in size, see **Fig.** 3.6. *In situ* AFM measurements were also performed, they have however not shown any interesting properties, due to the geometry of these experiments. The maximum scan size of the LiteScope AFM module is 80 µm, while the outer cladding of our fibers is 128 µm, therefore no overlap between the scanned area and modified area was achieveable.

The feedback of the probe did not behave in an different way even though gas was flowing through it. This can be explained by the probe geometry. Even though the tip itself is in contact mode with the sample substrate, the thin capillaries are several microns further, depending on the tip angle. The capillary faces were also cut in the same angle, changing the geometry in our simulations depicted in **Fig.** 2.1.

Neither of the samples fabricated in this manner exhibited any demonstrable change in stoichiometry when their Raman fingerprints were measured. Even though the modification site increased its volume compared to the starting thin film area, we still could not find optimal setup. Our hypothesis was that we have insufficient overlap of oxygen atmosphere and laser spot. This could be overcome by either shining light below the approached probe from a distance (to enable gas and laser light overlap), or by making a PM-1550-01 planar probe and using the single fiber methodology with a pre structured sample and keeping low laser light powers (below 50 mW, where the layer evaporates substantially). We have decided on changing the geometry of the two fiber manipulators, which seemed to be the less time-consuming solution of this problem. Using the fiber configuration 2.10b, we have done several experiments with the VFM fiber roughly 500 µm

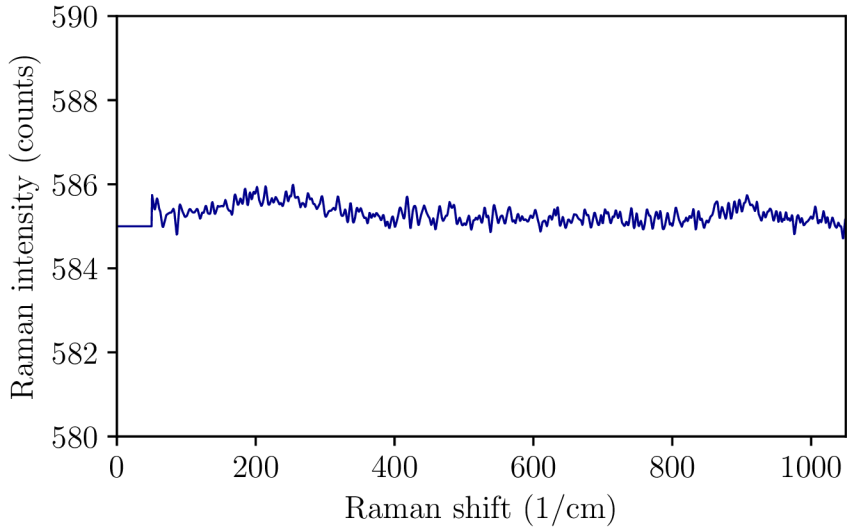

Fig. 3.5: Typical raman fingerprint of regions locally modified by the twin fiber manipulator method. Any change induced in the sample morphology did not show a different oxidation stat. The same results were shown for both alignment marks, made only while TFM fiber was in contact, and modification sites, made while close AFM probe (O_2 source) proximity was maintained.

from the sample surface and laser powers from 50 mW to 250 mW (we increased the laser power due to the longer fiber-surface distance).

Of all attempts at this local oxidation setup, only once have we seen something grow beneath our probe. This is mostly due to inadequate possibilities of verifying the light spot-O_2 atmosphere overlap. The tip-enhanced method could prove useful, if the amount of light coming inside the probe was quantified. We propose coupling light coming from the probe into a photomultiplier. That way, we could move the probe around, looking for maximal value of light reflected into it. A side product of such a setup would be *in situ* reflection measurements and correlation between topography, SEM image and light reflection of our sample. Preparation of such a method would be time consuming, as an aperture must be formed in the vanadium layer covering the tip (for light to be efficiently coupled outside the SEM chamber) as well as setting up both gas and light coupling via vacuum tubing. We have tried to solve both of these challenges in one go by taking a vanadium coated probe and coupling light into just as described in Section 2.2.1. Even though we could not tell how much light got through the PCF fiber, an estimate could be done using the copper sleeve. If the fiber coupling is not set up efficiently, most light can be seen reflected inside the sleeve or dispersed inside the fibers. Moving the two ferrules closer together should decrease the amount of reflected light until the two fibers touch, when the light is dispersed again. By employing this knowledge of our multifunctional gas injectional system, we managed to transfer enough laser light power to evaporate the thin vanadium film near the core of the fiber. This evaporation formed an aperture wide

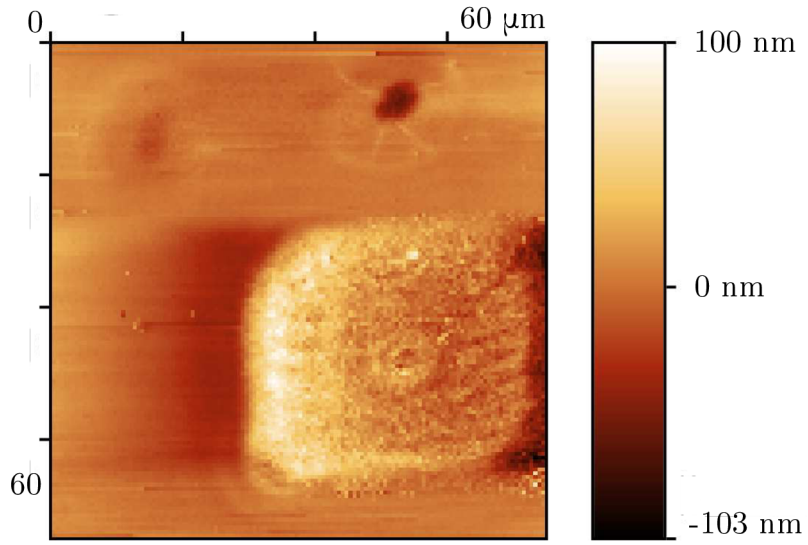

Fig. 3.6: Topography (scanning probe microscopy (SPM) image, LiteScope AFM) of $30 \times 30\,\mu m^2$ array at $P_{vis} = 50\,mW$. During the local heating by laser power, a hollow AFM probe brought oxygen into vicinity of the local oxidation site. The array is surrounded by an alignment mark made using only VFM fiber with $P_{max} = 75\,mW$ laser light power, with the hollow probe 10 mm away. The mark has a 100 nm hole in places with maximal laser dwell time, whereas the array is a 100 nm growth (atop 100 nm thin vanadium film on a fused silica substrate). This measurement was performed as the hollow AFM probe permeated oxygen molecules, hinting at sub-optimal localization of oxidation atmosphere.

enough for laser light to pass to potential sample surface or be detected outside the SEM microscope chamber. Such a probe can be suitable for Correlative Probe and Electron Microscopy (CPEM [61]), due to its conductive outer layer and light guiding aperture. Of course, the same effect could be done using a Focused Ion Beam (FIB) technique and the aperture would be smaller and better defined, but the high power laser light flashing took minutes to set up. For proof-of-concept this method seems adequate, but sacrificing lateral resolution does not outweigh the time consumption in the long run.

3.2.3 Local Oxidation using a Planar AFM Probe in SEM

During prior attempts at local oxidation of vanadium thin films inside the SEM chamber, several observations and conclusions were made. Most notably, the necessity of overlapping the O_2 local atmosphere and the laser light ($\lambda = 532\,nm$) spot (as discussed in Section 3.2.2) and the proximity of photonic crystal fiber's thin capillaries to the sample surface (discussed in Section 3.2.1). Combined with practical knowledge of the two photonic crystal fibers used within the scope of this thesis (discussed in Section 2.2), i.e. the time it takes for oxygen particles to permeate through the PCF fiber into the SEM vacuum chamber aswell as the amount of particles forming the local atmosphere, we have made several changes to the newly developed experimental setup of our unique

Local Oxidation Method within SEM chamber. We have made our AFM probe using the PM-1550-01 fiber. This meant optimal response of O_2 intake, but less laser light power output. We have cleaved the face of the PM-1550-01 fiber using a Thorlabs optical fiber cleaver, making the fiber face as planar as possible. Having a planar AFM probe meant topography measurements were non viable due to suboptimal lateral resolution and the probe itself was difficult to create in a way that would allow for approach into the sample surface vicinity.

After coupling roughly 15 % of input laser light power (see Section 2.2.1), we placed the custom made planar AFM probe into the LiteScope AFM module inside the SEM vacuum chamber. Our probe was able to approach and retract accordingly to the sample surface while our multifunctional gas injection system was empty. Once 6 bar of oxygen gas filled the multifunctional gas injection system tubing, the behavior of our planar AFM probe changed. While for probe-surface z distances over $z_{\text{lim}} = 50\,\mu\text{m}$, the resonant frequency of our probe remained the same, once we began approaching into contact with the probe, the probable increase of local O_2 atmosphere showed. Resonant frequency of our probe changed once close proximity was reached, meaning the nature of the AFM feedback loop changed and, instead of maintaining the probe-sample distance, the probe felt a growth forming below it. At this point, we stopped the automatic approach and measured the resonant curve again. Significant change in oscillation amplitude occurred

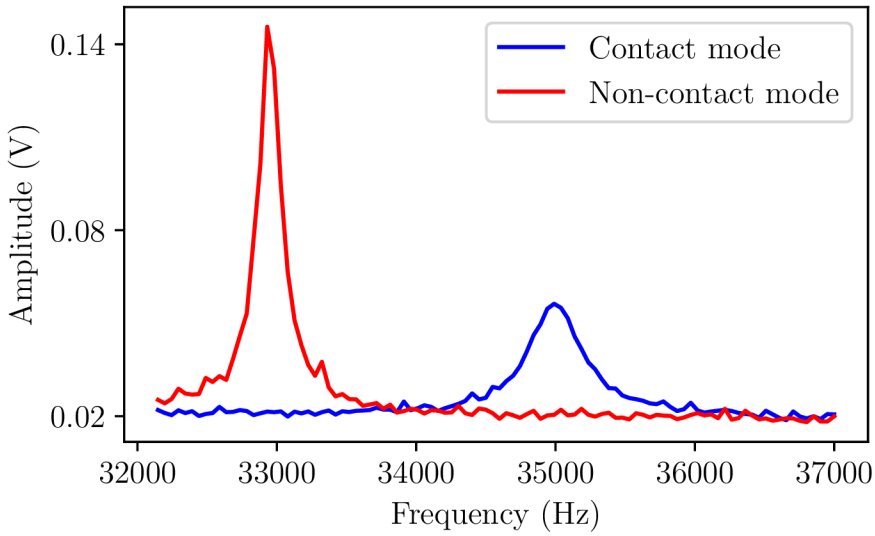

Fig. 3.7: Resonant frequency shift of a planar AFM probe made using the PM-1550-01 fiber. For probe-sample z distances larger than $z_{\text{lim}} = 50\,\mu\text{m}$ the planar probe resonant frequency is at $\omega_0 = 33\,\text{kHz}$ with the maximal oscillation amplitude being $A_0 = 0.14\,\text{V}$. If O_2 gas is allowed to permeate through the hollow fiber, this frequency can change. Once the probe approaches the sample surface using the piezo scanner (closer than z_{lim}), the resonant frequency shifts to $\omega_1 = 35\,\text{kHz}$, with the amplitude oscillation dampened to $A_1 = 0.05\,\text{V}$.

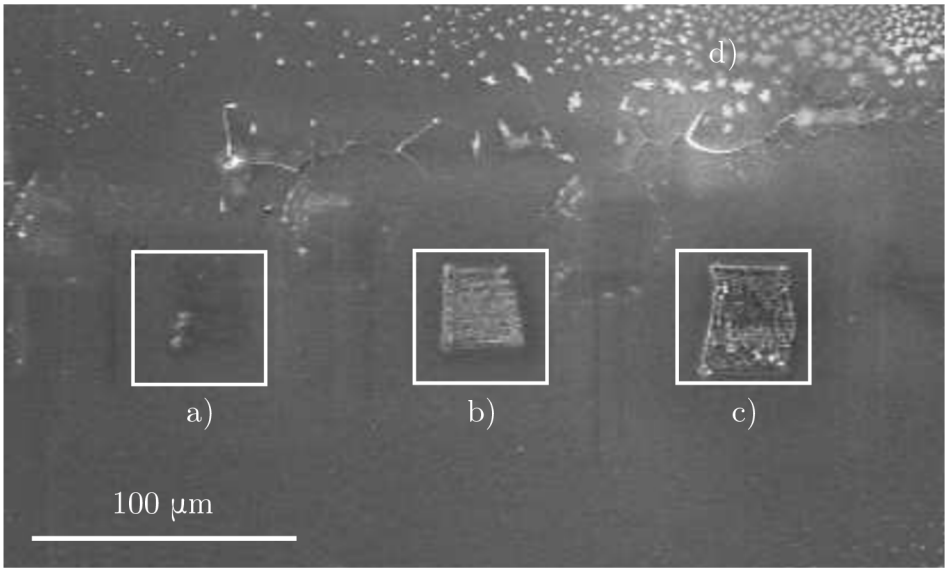

Fig. 3.8: Three locally oxidized $30 \times 30\,\mu m^2$ arrays with dwell time corresponding 64 ppl: a) array modified using 15 mW laser light power, b) array modified by 20 mW laser light power, c) array modified by 25 mW laser light power. Pressure in the multifunctional gas injection system was kept constant at 6 bar of O_2, with PM-1550-01 fiber used as a planar AFM probe of LiteScope SPM. For 15 mW laser light power output only regions where the probe remained for extended periods of time are visibly modified. For 25 mW the modification is inhomogeneous, with visible cracks forming inside the oxidation site. 20 mW laser light power used seems to yield the best results in terms of homogeneous oxidation site growth. After c) array oxidation was done, parasitic oxidation sites began to show d). These parasitic oxidation sites were symmetrical over a region corresponding to the PM-1550-01 fiber cross-section. After local oxidation the sample was characterized using optical microscopy, where the parasitic sites were no longer visible. Further characterizations included AFM topography measurements to characterize growth type and Raman spectroscopy to characterize optical response of changes in the composition of locally modified vanadium films

while in close proximity, with value below half of initial amplitude (see **Fig.** 3.7), indicating a denser atmosphere near the tip of the AFM probe. The resonant frequency of oscillations also changed from 33 kHz to 35 kHz, indicating a change of either probe mass or probe-surface friction. This quite new effect of resonant frequency shift caused by local atmospheric increase and planar probe sample surface configuration was perfectly reproducible, with exactly the same outcomes occurring whenever the planar AFM probe approached the sample surface. A viable hypothesis can be that the Knudsen number (Kn, see Section 2.1) changes due to characteristic length shrinking while the planar AFM probe comes into contact mode. The more frequent collisions between the oxygen particles and probe-sample system then cause the difference in both amplitude and location of resonant frequency.

It was now clear the local oxidation system has changed significantly from our prior experiments. We have therefore started our local oxidation experiments using a planar AFM probe on a laser beam pre-structured (see Section 2.4) vanadium sample surface from the lowest laser light powers possible.

Three $30 \times 30\,\mu m^2$ arrays were made using 15 mW, 20 mW, and 25 mW as starting laser light powers. All three modifications made using 64 ppl clearly visible while imaging in SEM (see **Fig.** 3.8). For the lowest laser light output power, only regions where the probe ramained at the start (during initial laser light power calibration) were visible while SEM imaging (at 5 kV accelerating voltage). Additional dwell time characterization would be beneficial, due to the significant change the local oxidation experiments have gone through since we first started. For 15 mW, the oxidation site seems most homogeneous of the three, with the probable cause being the ratio of dwell time and laser power reached. For 25 mW, the oxidation site can be seen nicely while imaging in SEM, but it also started visibly cracking. We have to therefore provide enough heat via the laser light power output into the thin vanadium layer (on quartz substrate) for oxidation to take place, but also enough time for the modification to incorporate in a homogeneous way. We can see changes will happen even for lower laser light output power (**Fig.** 3.8), but only when the probe dwells for extensive periods of time. On the other hand, if we induce too much heat inside the thin film without a chance of transferring it in a homogeneous way, (too much laser light power over time), the layer will crack and oxidation sites will be inhomogeneous as can be seen above the three locally oxidized arrays.

Surrounding the three arrays were additional oxidation sites that were not present on the layer prior to local oxidation experiments. The shape of these parasitic oxidation sites reminded us of macroscopic oxidation sites we have seen when the thin films oxidized quickly due to vanadium target impurities (as discussed in Section 3.1). The parasitic oxidation sites were not visible using conventional optical microscopes however, so no deeper study as to what they were was conducted.

After the local oxidation within the SEM vacuum chamber was done, additional *ex situ* AFM and optical characterization of the three modification sites followed. AFM measurements could not be done with LiteScope AFM module since the AFM probe used to locally oxidize our sample was planar and its lateral resolution inadequate. For topography measurements, we have therefore opted to use the Scanning Probe Microscope Bruker Dimension Icon. For optical characterization Witec Alpha 300R was used. Both of these instruments are located at CEITEC Nano Research Infrastructure, BUT.

For 15 mW, AFM measurement gave us the following results: The oxidation site grew by 400 nm (see **Fig.** 3.9) only at a region that wes exposed to laser light for an extended period of time (due to tuning of laser light power output that was done prior to scanning). Even though the laser light remained only at one place, three oxidation sites have been created during this period. These oxidation sites were circles of roughly 5 µm in diameter, hinting at a possible correlation between the PM-1550-01 fiber panda cross-section. In contact mode, we expect most oxygen particles coming from the fiber to be near the thin capillary (as we discussed in Section 2.1). We can therefore assign the two outer oxidation sites to correlate with a dense O_2 atmosphere, with enough energy due to proximity of the middle oxidation site (where the laser light was focused). This entire geometry of three oxidation sites is elongated due to the angle of capillary face and sample surface. This can show us regions of maximal sample modification for our probe-sample system. Therefore, local oxidation of the sample without moving the probe provided us with useful information about our system and can serve as a reference for later oxidation experiments.

We then measured Raman spectra on the 15 mW modified region. We used a 532 nm laser focused by a 100 x objective for optimal lateral resolution. We first measured the entire local oxidation region, mapping Raman spectra in each point. We found 10 peaks corresponding to V_2O_5 modes in the middle of the oxidation site with maximal laser dwell time (this is due to the gaussian profile of our laser beam).

The V_2O_5 peaks were located at 98 cm^{-1}, 141 cm^{-1}, 196 cm^{-1}, 281 cm^{-1}, 299 cm^{-1}, 406 cm^{-1}, 467 cm^{-1}, 529 cm^{-1}, 700 cm^{-1} and 992 cm^{-1}. Other modified regions exhibited a VO_2 rutile phase, with no V_2O_5 peaks found in the other two oxidation sites. From the spectral

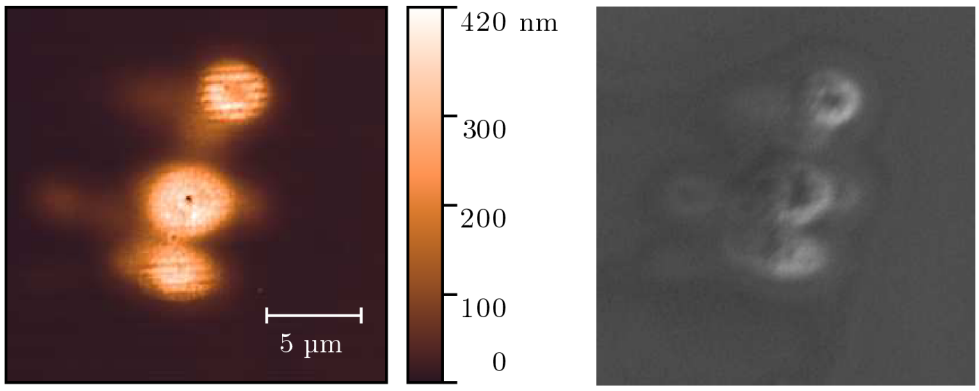

Fig. 3.9: AFM topography measurement (a) and SEM image (b) of locally oxidized region. A planar PCF 1550-01 AFM probe was brought into contact with vanadium sample surface using the LiteScope approach function. With both light and O_2 coupled into the probe, we oxidized the V surface with 15 mW laser light power output and 6 bar pressure difference. Middle oxidation site corresponds to location of maximal laser light power and side oxidation sites correspond to location of maximal oxygen intake, as per the PM-1550-01 panda structure.

information we could see that V-VO_2-V_2O_5 sites are cleary visible when mapping the 1000 cm^{-1} Raman shift region, as pure vanadium in this region has low Raman intensity, the rutile VO_2 fingerprint (see **Fig.** 3.10 d, dark red) has a broad peak at 500 cm^{-1} with medium Raman intensity still detectable at 992 cm^{-1} and V_2O_5 Raman fingerprint (see **Fig.** 3.10 b) has a sharp peak at 992 cm^{-1}. We therefore decided on characterizing this oxidation region by the value located near the peak in an interval (992 ± 5) cm^{-1} summing the amount of counts when creating spectral maps (see **Fig.** 3.10 a).

We then decreased the laser light power (to 0.2 mW) to return the VO_2 phase back into a monoclinic phase, with one broad peak visible at. We opted against mapping the Raman spectra in the entire oxidation region, as the integration time to obtain adequate signal to noise ratio would be several minutes per one scanned point. We would take single spectrum multiple times in regions previously characterized with VO_2 rutile Raman fingerprint. We found nine VO_2 peaks 142 cm^{-1}, 192 cm^{-1}, 223 cm^{-1}, 260 cm^{-1}, 308 cm^{-1}, 339 cm^{-1},

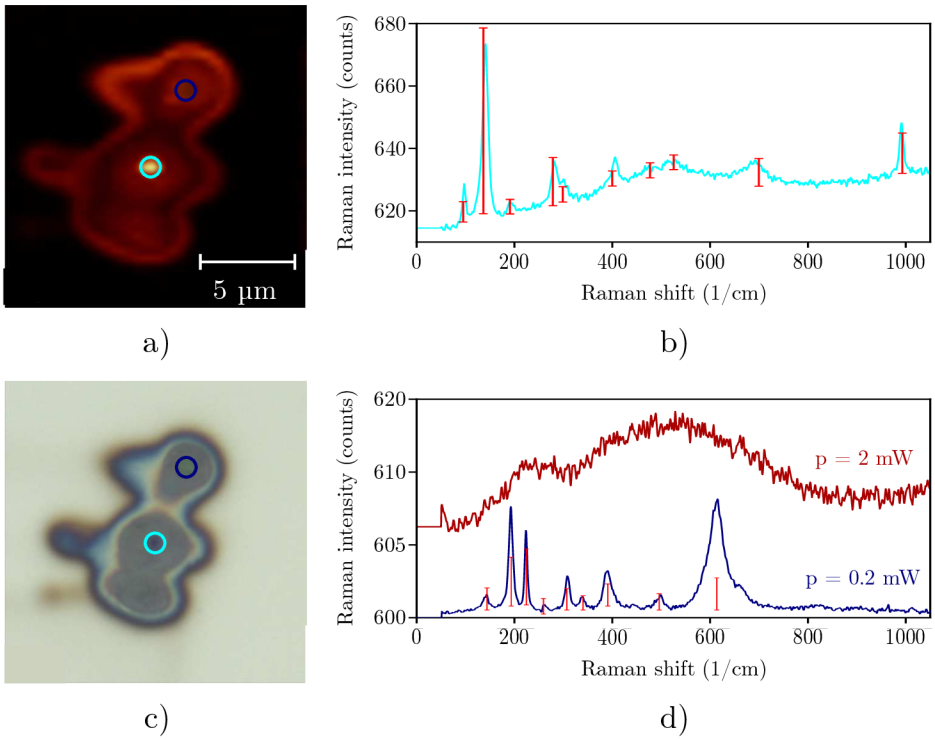

Fig. 3.10: Raman fingerprint scan (a) and optical microscope image (c) of locally oxidized region $P = 15$ mW by a PM-1550-01 AFM probe. For the center of the laser beam (light blue circle in both a) and c) the vanadium sample was oxidized to V_2O_5 b). The Raman spectra is compared to V_2O_5 from [62]. Other regions (dark blue circle) show a rutile VO_2 (dark red, d) phase due to induced phase change by the Raman laser power $P = 2$ mW. Once the laser power was reduced to $P = 0.2$ mW Raman fingerprint of monoclinic phase of VO_2 was visible (dark blue, d) and compared to [62] The Raman spectral map a) focuses on the 992 cm^{-1} shift region, distinguishing between vanadium (black), VO_2 (red) and V_2O_5 (yellow).

390 cm^{-1}, 494 cm^{-1} and 992 cm^{-1} corresponding to its monoclinic phase (see **Fig.** 3.10 d, dark blue).

The modification when using a longer dwell time with a lower laser power was intriquing, we saw that we could obtain mostly a singular vanadium oxide stoichiometry, with only a singular region showing a V_2O_5 oxidation state. We also discovered that perfect laser light O_2 atmosphere overlap is not completely necesarry if we provide a dense enough atmosphere, with two oxidation sites created on the sides of the laser spot.

The 20 mW locally modified array was then subjected to the same characterization. AFM topography measurements revealed that the oxidation site was even higher than the growth found at 15 mW oxidation region (see **Fig.** 3.11), with up to 600 nm growth found on top of the 100 nm thin vanadium film. Such a growth is unexpected, if we take into consideration a simple volume increase resulting in vanadium atom binding two oxygen atoms to it, we should see the layer double in size, providing every vanadium atom reacts and the growth is homogeneous. A possible explanation is the fact that the growth itself can be porous, meaning some places can grow more with overall mass conservation. Another effect we can add to this is the fact that even when no oxygen was present, the modified layer grew twice in size as a result of the cracking and binding vanadium from around the modification site, forming a meniscus near the edges (see **Fig.** 3.6). We could see that the left and right edge has a porous "canyon" like shape, this is probably

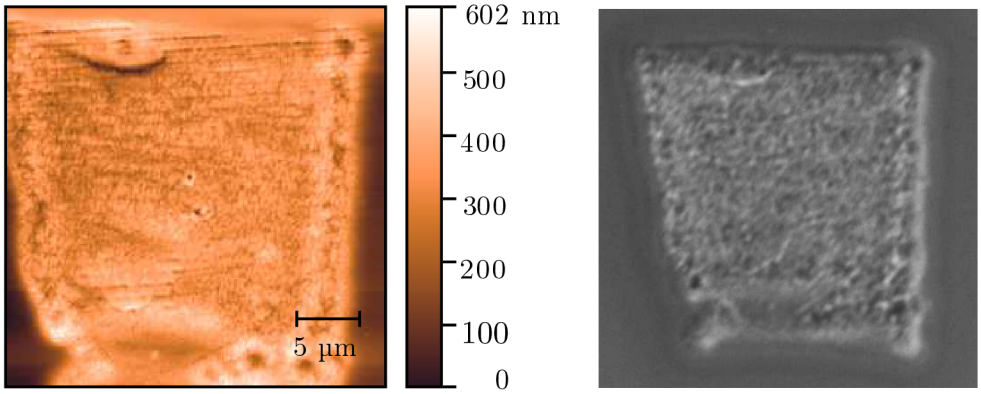

Fig. 3.11: AFM topography measurement (a) and SEM image (b) of locally oxidized region. A planar PCF 1550-01 AFM probe was brought into contact with vanadium sample surface using the LiteScope approach function. With both light and O_2 coupled into the probe, we oxidized the vanadium surface with 20 mW laser light power output and 6 bar pressure difference. The oxidation region was designed as a $30 \times 30\,\mu m^2$. The modified area grew most (up to 600 nm) in regions with maximal dwell time (left and right edges). The oxidation region is slanted due to the face of the AFM probe and sample surface not being perfectly parallel. The oxidation site is more porous compared to its lower laser light power output counterpart, indicating at optimal dwell time necessity that will be further studied in the future.

explained by the trace-retrace AFM probe direction change, meaning the probe spends most time in these edges.

Raman spectroscopy of the 20 mW locally oxidized region followed. We firstly mapped the Raman fingerprints of the entire region to have complete information of what vanadium oxide stoichiometries we can expect and measure (if any). Similarly to 15 mW modified region, we have mostly seen rutile VO_2 peaks (see **Fig.** 3.12), with some areas (that were exposed to laser light during local oxidation for extended periods of time due to laser light power output calibration) stoichiometry showing V_2O_5 peaks. We have again characterized our Raman fingerprint scan by the V_2O_5 peak located at 992 cm^{-1} as we can

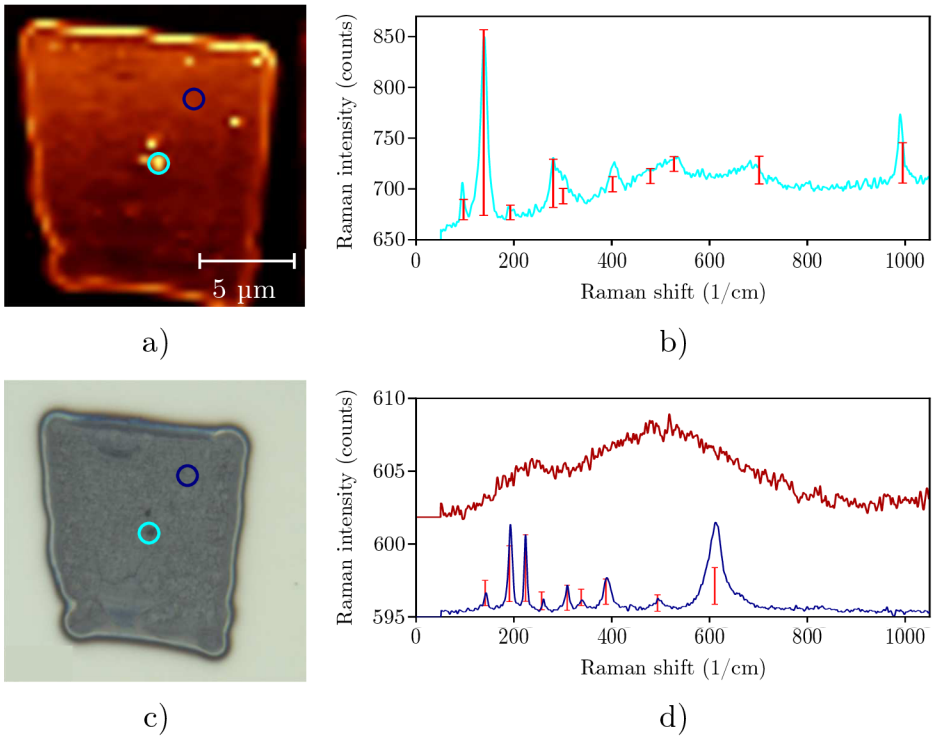

Fig. 3.12: Raman fingerprint scan (a) and optical microscope image (c) of locally oxidized region $P = 20$ mW by a PM-1550-01 AFM probe. For the center of the laser light output calibration (light blue circle in both a) and c) the vanadium sample was oxidized to V_2O_5 b), the Raman spectra (b) is compared to V_2O_5 from [62]. Other regions (dark blue circle) show broad, rutile VO_2 peaks due to phase change induced by the Raman laser light power ($P = 2$ mW). The Raman spectral map a) focuses on the 992 cm^{-1} shift region, distinguishing between V (black), VO_2 (red) and V_2O5 (yellow). We can see the edges contain most of the V_2O_5 phase. This can be explained by their maximal laser dwell time over a short period of time during the AFM probe trace-retrace motion change. Raman spectra of regions inside dark blue circle (top right a, c) showed VO_2 phase transition from monoclinic (blue, $P = 0.2$ mW) to rutile (red, $P = 2$ mW) phase induced by incrementing laser light power. Positions and relative intensities of monoclinic VO_2 Raman peaks are compared to VO_2 Raman spectrum found in literature [62].

easily distinguish pristine vanadium, VO_2 and V_2O_5. This helped us identify rutile VO_2 phase (see **Fig.** 3.12 d, red), where we reduced the incident laser light power to 0.2 mW and measured the spectra again, showing a monoclinic phase of VO_2 (see **Fig.** 3.12d, blue). Both monoclinic VO_2 and V_2O_5 spectra were compared to Raman fingerprints of the same materials studied in literature [62].

Finally, the 25 mW locally oxidized region was characterized in the same way as its counterparts. Both SEM and AFM topography imaging proved that the resulting oxidation site was inhomogeneous and porous (see **Fig.** 3.13) and the shape of the oxidation site was unexpected. The slightly slanted shape (we have seen during prior experiments), caused by the AFM probe-sample surface geometry, was modified further. Adding the novel shape with the oxidation site inhomogenity, we expect a vanadium residue formed on the planar AFM probe during local oxidation. This residue scattered incident laser light into different directions and, due to the local O_2 atmosphere, modified the sample surface further away from the scanned area in a less defined manner.

We again see the benefit of having lower laser light powers balanced by longer local oxidation site dwell times. The maximal growth on the oxidation site was around 700 nm, this is again most likely due to the porous nature of the growth, but further characterization and exploration of the oxidation structure is required.

Measuring Raman spectra of the 25 mW oxidation site showed again both V_2O_5 and VO_2 was locally obtained on the vanadium surface (see **Fig.** 3.14). This time it was more difficult to determine why some regions were VO_2 and why others V_2O_5 due to the aforementioned change in geometry. The subtle gradual decrease in Raman intensity as we go further down the scan direction confirmed the hypothesis of residual vanadium forming due to too high laser light powers. The residue most likely formed during the first

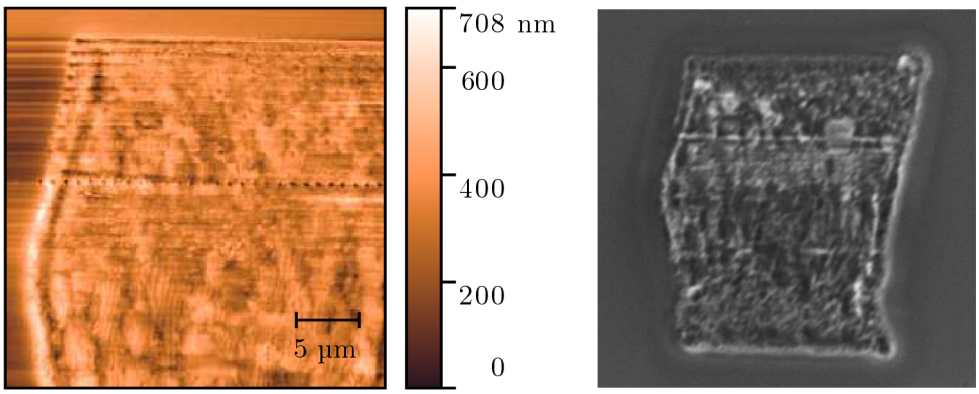

Fig. 3.13: AFM topography measurement (a) and SEM image (b) of locally oxidized region. A planar PCF 1550-01 AFM probe was brought into contact with vanadium sample surface using the LiteScope approach function. With both light and O_2 coupled into the probe, we oxidized the V surface with 25 mW laser light power output and 6 bar pressure difference. The oxidation region was designed as a 30×30 µm.

line (probably the dotted line of etched holes consisting of mostly V_2O_5) and scattered the laser light in the y direction. It was still possible to see both monoclinic and rutile VO_2 phases while measuring Raman fingerprints.

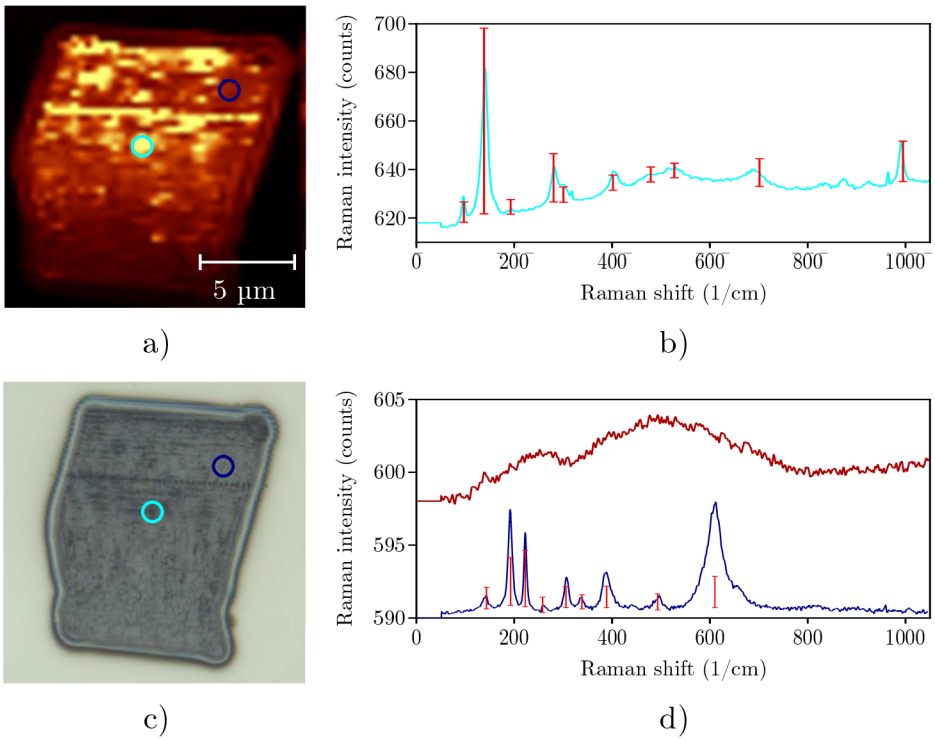

Fig. 3.14: Raman fingerprint scan (a) and optical microscope image (c) of locally oxidized region with $p = 25\,\mathrm{mW}$ by a PM-1550-01 planar AFM LiteScope probe. The Raman spectra (b), yellow regions of (a), is compared to V_2O_5 from [62]. Other regions (dark blue circle) show broad, rutile VO_2 peaks due to phase change induced by the Raman laser light power ($p = 2\,\mathrm{mW}$). The Raman spectral map a) focuses on the $992\,\mathrm{cm}^{-1}$ shift region, distinguishing between V (black), VO_2 (red) and V_2O_5 (yellow). We can see the edges surprisingly do not contain most of the V_2O_5 phase, but due to the different geometry, it is difficult to say where the AFM probe was during the laser light power calibration. There is also no way of knowing how the laser light spot looked during local oxidation, as vanadium residue most likely formed on the AFM probe. The hypothesis of residue formation and subsequent laser ligh power output decrease is supported by the lowering in Raman intensity the further in the scan direction we go. Most V_2O_5 is located near the line of etched holes of unknown origin. Raman spectra (d) of regions inside dark blue circle (top right a, c) showed VO_2 phase transition from monoclinic (blue, $p = 0.2\,\mathrm{mW}$), to rutile (dark red, $p = 2\,\mathrm{mW}$) phase induced by incrementing laser light power. Positions and relative intensities of monoclinic VO_2 Raman peaks are compared to VO_2 Raman spectrum found in literature [62]

CONCLUSIONS

The presented diploma thesis is dedicated to development, implementation and characterization of a novel way of locally oxidizing vanadium-based samples. It consists of three main parts. Chapter 1 is dedicated to IBAD of thin vanadium samples, possible stoichiometry modification methods and optical characterization of vanadium oxides found within this diploma thesis. Chapter 2 describes the development a realization of two novel possible methods for locally modifying vanadium-based thin films inside the SEM vacuum chamber. Both methods are based around possibilities of bringing both laser light and a local O_2 atmosphere via photonic crystal fibers. For this purpose, we have modified SEM Vega to accommodate a multi-functional gas injection system. We have shown that gas intake possibilities of two PCFs used within this thesis depends on the diameter of its capillaries, with residual gas analysis of O_2 flow capabilities resulting in favor of the PM-1550-01 fiber. We have also done Monte Carlo simulations of O_2 particles flowing from a thin capillary. We have shown that sample-capillary distance is crucial, with the local atmosphere being the most dense in near contact mode. We have then used this knowledge in the experimental part 3, where we locally oxidized vanadium based thin films. We have began by single fiber manipulator method with LMA-5 fiber, which, due to its narrow capillaries, proved unable to locally oxidize region in a desirable manner. We then moved on to the twin fiber manipulator method, where we tested various fiber configurations. One fiber would bring laser light into the vacuum chamber (via the VFM) and the other would serve as a gas injection system/AFM probe (via LiteScope AFM module). The twin fiber manipulator method proved unsuccessful at locally modifying oxidation state of vanadium based thin films, mainly due to difficulties associated with overlapping of O_2 atmosphere and laser light spot. A new slightly modified version of the single fiber manipulator method was therefore developed, with PM-1550-01 fiber used to bring both O_2 gas and laser light to the vanadium based samples. The face of the fiber was cut as planar as possible, to ensure optimal capillary-sample surface proximity. The PM-1550-01 fiber proved its potential of bringing both O_2 gas and laser light into, as the local O_2 atmosphere was confirmed by a significant resonant frequency change while approaching the sample surface with the AFM probe. Three locally oxidized regions were made using this method and optically characterized by Raman spectroscopy after fabrication was done. We have obtained local sites of vanadium oxides on our pristine vanadium sample, with both rutile and monoclinic VO_2 phases detected along with V_2O_5 phase for regions modified with higher laser light powers. The novel local oxidation method within SEM vacuum chamber therefore was therefore proved successful and stands, to the best of our knowledge, as a unique way of locally obtaining vanadium oxides.

BIBLIOGRAPHY

1. HARPER, JME; CUOMO, JJ; KAUFMAN, HR. Technology and applications of broad-beam ion sources used in sputtering. Part II. Applications. *J. Vac. Sci. Technol.* 1982, vol. 21, no. 3, pp. 737–756.

2. ŠIKOLA, Tomáš; SPOUSTA, Jiří; DITTRICHOVÁ, Libuše. Equipment for Modification, Etching and deposition of Thin Films Based on a Broad Beam Ion Source. *Scripta Fac. Sci. Nat. Univ. Masaryk.* 1992, vol. 22, pp. 119–137.

3. SEAH, MP; NUNNEY, TS. Sputtering yields of compounds using argon ions. *Journal of Physics D: Applied Physics.* 2010, vol. 43, no. 25, p. 253001.

4. YIN, W et al. The metal-insulator transition in vanadium dioxide: A view at bulk and surface contributions for thin films and the effect of annealing. *Journal of Applied Physics.* 2009, vol. 105, no. 11.

5. PICCIRILLO, C.; BINIONS, R.; PARKIN, I.P. Synthesis and Functional Properties of Vanadium Oxides: V2O3, VO_2, and V_2O_5 Deposited on Glass by Aerosol-Assisted CVD. *Chemical Vapor Deposition.* 2007, vol. 13, no. 4, pp. 145–151. available from DOI: https://doi.org/10.1002/cvde.200606540.

6. BUKHARI, Syed A. et al. The effect of oxygen flow rate on metal–insulator transition (MIT) characteristics of vanadium dioxide (VO_2) thin films by pulsed laser deposition (PLD). *Applied Surface Science.* 2020, vol. 529, p. 146995. available from DOI: https://doi.org/10.1016/j.apsusc.2020.146995.

7. ZHANG, Dong-ping et al. High performance VO_2 thin films growth by DC magnetron sputtering at low temperature for smart energy efficient window application. *Journal of Alloys and Compounds.* 2016, vol. 659, pp. 198–202. available from DOI: https://doi.org/10.1016/j.jallcom.2015.11.047.

8. ZHANG, Yanqing; XIONG, Weiming; CHEN, Weijin; ZHENG, Yue. Recent Progress on Vanadium Dioxide Nanostructures and Devices: Fabrication, Properties, Applications and Perspectives. *Nanomaterials.* 2021, vol. 11, no. 2. available from DOI: 10.3390/nano11020338.

9. PERGAMENT, A. L. Metal-Insulator Transition Temperatures and Excitonic Phases in Vanadium Oxides. *ISRN Condensed Matter Physics.* 2011, vol. 2011, p. 605913. available from DOI: 10.5402/2011/605913.

10. LEE, D. et al. Isostructural metal-insulator transition in VO_2. *Science.* 2018, vol. 362, no. 6418, pp. 1037–1040. available from DOI: 10.1126/science.aam9189.

11. DUONG, Hoang; WILSON, Robert; LIANG, Daniel. Solid-State Reduction of Vanadium Pentoxide by Hydrogen. *Available at SSRN 4479254.* 2023. available from DOI: https://doi.org/10.1016/S0022-0728(80)80023-4.

12. XU, Shi; EVANS, B.L.; FLYNN, David I.; EN, Cao. The study of island growth of ion beam sputtered metal films by digital image processing. *Thin Solid Films.* 1994, vol. 238, no. 1, pp. 54–61. available from DOI: https://doi.org/10.1016/0040-6090(94)90648-3.

13. JOYCE, B.A et al. Nucleation mechanisms during MBE growth of lattice-matched and strained III–V compound films. *Applied Surface Science.* 1998, vol. 130-132, pp. 357–366. available from DOI: https://doi.org/10.1016/S0169-4332(98)00084-1.

14. STEFANOVICH, GB; PERGAMENT, AL; VELICHKO, AA; STEFANOVICH, LA. Anodic oxidation of vanadium and properties of vanadium oxide films. *Journal of Physics: Condensed matter.* 2004, vol. 16, no. 23, p. 4013.

15. LI, Jing-Mei; CHANG, Kuo-Hsin; HU, Chi-Chang. The key factor determining the anodic deposition of vanadium oxides. *Electrochimica Acta*. 2010, vol. 55, no. 28, pp. 8600–8605. available from DOI: https://doi.org/10.1016/j.electacta.2010.07.094.

16. KOZHUKHOV, A. S.; SCHEGLOV, D. V.; FEDINA, L. I.; LATYSHEV, A. V. The initial stages of atomic force microscope based local anodic oxidation of silicon. *AIP Advances*. 2018, vol. 8, no. 2, p. 025113. available from DOI: 10.1063/1.5007914.

17. BARTOŠÍK, Miroslav et al. Role of humidity in local anodic oxidation: A study of water condensation and electric field distribution. *Phys. Rev. B*. 2009, vol. 79, p. 195406. available from DOI: 10.1103/PhysRevB.79.195406.

18. CAMBEL, Vladimír; ŠOLTÝS, Ján. The influence of sample conductivity on local anodic oxidation by the tip of atomic force microscope. *Journal of Applied Physics*. 2007, vol. 102, no. 7.

19. KOZHUKHOV, AS; SCHEGLOV, DV; FEDINA, LI; LATYSHEV, AV. The initial stages of atomic force microscope based local anodic oxidation of silicon. *AIP Advances*. 2018, vol. 8, no. 2.

20. KOMONOV, Aleksandr I; MANTSUROV, Nikita D; MUTILIN, Sergey V; VOLOSHIN, Bogdan V; SELEZNEV, Vladimir A. Nanolithography of Amorphous Vanadium Oxide Films Using an Atomic Force Microscope. 2022, pp. 20–24.

21. BANDHU, Hemadri; ASHOK, P; KHANDAPU, Durga Prasad; VERMA, Amit. Lithography-free fabrication of Vanadium Dioxide and its devices using direct laser writing. *Optics & Laser Technology*. 2023, vol. 167, p. 109673.

22. SEO, Giwan et al. Facile photothermal synthesis of localized vanadium oxide capable of extraordinary phase transition. *Optical Materials Express*. 2017, vol. 7, no. 8, pp. 2860–2870.

23. VILANOVA-MARTÍNEZ, Paloma; HERNÁNDEZ-VELASCO, Jorge; LANDA-CÁNOVAS, AR; AGULLÓ-RUEDA, F. Laser heating induced phase changes of VO_2 crystals in air monitored by Raman spectroscopy. *Journal of Alloys and Compounds*. 2016, vol. 661, pp. 122–125.

24. IVANOV, VG; ILIEV, MN; THOMSEN, C. Micro-Raman study of isotope substitution in YBa 2 Cu 3 18 O 6.2 during local laser annealing. *Physical Review B*. 1995, vol. 52, no. 18, p. 13652.

25. BERGLUND, CN; GUGGENHEIM, HJ. Electronic Properties of V O 2 near the Semiconductor-Metal Transition. *Physical Review*. 1969, vol. 185, no. 3, p. 1022.

26. JUNG, WD; SCHMIDT, FA; DANIELSON, GC. Thermal conductivity of high-purity vanadium. *Physical Review B*. 1977, vol. 15, no. 2, p. 659.

27. LIU, Kunxiang; ZHAO, Qi; LI, Bei; ZHAO, Xia. Raman spectroscopy: A novel technology for gastric cancer diagnosis. *Frontiers in Bioengineering and Biotechnology*. 2022, vol. 10, p. 856591.

28. CHOI, Songhee; CHANG, Sung-Jin; OH, Junhyeob; JANG, Jae Hyuck; LEE, Shinbuhm. Electrical and Optical Properties of VO_2 Polymorphic Films Grown Epitaxially on Y-Stabilized ZrO2. *Advanced Electronic Materials*. 2018, vol. 4, no. 6, p. 1700620.

29. MENDIALDUA, J; CASANOVA, R; BARBAUX, YJJOES. XPS studies of V_2O_5, V6O13, VO_2 and V_2O_3. *Journal of Electron Spectroscopy and Related Phenomena*. 1995, vol. 71, no. 3, pp. 249–261.

30. DZHAGAN, VM et al. Raman fingerprints of different vanadium oxides as impurity phases in VO_2 films. *Optical Materials*. 2024, vol. 148, p. 114894.

31. HUPP, Joseph T; WILLIAMS, Robert D. Using resonance Raman spectroscopy to examine vibrational barriers to electron transfer and electronic delocalization. *Accounts of chemical research*. 2001, vol. 34, no. 10, pp. 808–817.

32. SMITH, Helen MJ. The theory of the vibrations and the Raman spectrum of the diamond lattice. *Philosophical Transactions of the Royal Society of London. Series A, Mathematical and Physical Sciences*. 1948, vol. 241, no. 829, pp. 105–145.

33. BENDTSEN, Jørgen. The rotational and rotation-vibrational Raman spectra of 14N2, 14N15N and 15N2. *Journal of Raman Spectroscopy*. 1974, vol. 2, no. 2, pp. 133–145.

34. SHVETS, Petr; DIKAYA, Olga; MAKSIMOVA, Ksenia; GOIKHMAN, Alexander. A review of Raman spectroscopy of vanadium oxides. *Journal of Raman spectroscopy*. 2019, vol. 50, no. 8, pp. 1226–1244.

35. UREÑA-BEGARA, Ferran; CRUNTEANU, Aurelian; RASKIN, Jean-Pierre. Raman and XPS characterization of vanadium oxide thin films with temperature. *Applied Surface Science*. 2017, vol. 403, pp. 717–727.

36. SRIVASTAVA, Ramakant; CHASE, LL. Raman Spectrum of Semiconducting and Metallic VO_2. *Physical Review Letters*. 1971, vol. 27, no. 11, p. 727.

37. ZHANG, Yifu; ZHENG, Jiqi; HU, Tao; TIAN, Fuping; MENG, Changgong. Synthesis and supercapacitor electrode of VO_2 (B)/C core–shell composites with a pseudocapacitance in aqueous solution. *Applied Surface Science*. 2016, vol. 371, pp. 189–195.

38. HOU, Jiwei; ZHANG, Jianwu; WANG, Zhongping; ZHANG, Zengming; DING, Zejun. Structural transition of VO 2 (A) nanorods studied by vibrational spectroscopies. *RSC Advances*. 2014, vol. 4, no. 35, pp. 18055–18060.

39. KAWAKUBO, Tatsuyuki; NAKAGAWA, Takehiko. Phase transition in VO_2. *Journal of the Physical Society of Japan*. 1964, vol. 19, no. 4, pp. 517–519.

40. LYSENKO, S et al. Light-induced ultrafast phase transitions in VO_2 thin film. *Applied Surface Science*. 2006, vol. 252, no. 15, pp. 5512–5515.

41. BASU, Raktima; SARDAR, Manas; DHARA, Sandip. Origin of phase transition in VO_2. in: *AIP Conference Proceedings*. AIP Publishing, 2018, vol. 1942. no. 1.

42. STEFANOVICH, G; PERGAMENT, A; STEFANOVICH, DJJoPCM. Electrical switching and Mott transition in VO_2. *Journal of Physics: Condensed Matter*. 2000, vol. 12, no. 41, p. 8837.

43. QUACKENBUSH, Nicholas F et al. Reducing orbital occupancy in VO_2 suppresses Mott physics while Peierls distortions persist. *Physical Review B*. 2017, vol. 96, no. 8, p. 081103.

44. LEE, D et al. Isostructural metal-insulator transition in VO_2. *Science*. 2018, vol. 362, no. 6418, pp. 1037–1040.

45. AKANDE, Amos A; DHONGE, BP; MWAKIKUNGA, Bonex W; MACHATINE, AGJ. Gate voltage controlled humidity sensing using MOSFET of VO_2 particles. 2017.

46. *Optical measurement detection unit: Cathodoluminescence* [http://surfaces.fme.vutbr.cz/laboratories/developed-instruments/2022-/]. 2024.

47. KNUDSEN, Martin. Die Gesetze der Molekularströmung und der inneren Reibungsströmung der Gase durch Röhren. *Annalen der Physik*. 1909, vol. 333, no. 1, pp. 75–130. available from DOI: https://doi.org/10.1002/andp.19093330106.

48. NAVIER, C. L. Sur les Lois du Mouvement des Fluides. *Mémoires L'Académie des Sci. L'institut Fr.* 1822.

49. ZHANG, Wen-Ming; MENG, Guang; WEI, Xueyong. A review on slip models for gas microflows. *Microfluidics and nanofluidics*. 2012, vol. 13, pp. 845–882.

50. TAITEL, Yemada; DUKLER, Abe E. A model for predicting flow regime transitions in horizontal and near horizontal gas-liquid flow. *AIChE journal*. 1976, vol. 22, no. 1, pp. 47–55.

51. BIRD, Graeme Austin. Molecular gas dynamics. *NASA STI/Recon Technical Report A*. 1976, vol. 76, p. 40225.

52. ARGÖNÜL, Aykut; KEIL, Frerich. An alternative procedure for modeling of Knudsen flow and surface diffusion. *Periodica Polytechnica Chemical Engineering*. 2008, vol. 52, pp. 37–55. available from DOI: 10.3311/pp.ch.2008-2.01.

53. *NKT photonics* [https://www.nktphotonics.com/products/optical-fibers-and-modules/large-mode-area-photonic-crystal-fibers/]. [n.d.].

54. *Thorlabs* [https://www.thorlabs.com/thorproduct.cfm?partnumber=PM-1550-01]. [n.d.].

55. *laser company Changchun New Industries Optoelectronics China, model MGL-FN-532* [www.cnilaser.com]. [n.d.].

56. ČERNEK, Ondrej. Use of a special optical fiber in an electron microscope chamber. *Bachelor thesis, BUT*. 2019.

57. *Nenovision* [https://www.nenovision.com/products/litescope-afm-in-sem]. [n.d.].

58. VERMA, Prabhat. Tip-Enhanced Raman Spectroscopy: Technique and Recent Advances. *Chemical Reviews*. 2017, vol. 117, no. 9, pp. 6447–6466. available from DOI: 10.1021/acs.chemrev.6b00821.

59. *Material of the Month: Fused Silica* [https://www.swiftglass.com/blog/material-month-fused-silica/]. 2024.

60. YAMASUE, Eiji; SUSA, Masahiro; FUKUYAMA, Hiroyuki; NAGATA, Kazuhiro. Thermal conductivities of silicon and germanium in solid and liquid states measured by non-stationary hot wire method with silica coated probe. *Journal of crystal growth*. 2002, vol. 234, no. 1, pp. 121–131.

61. NOVOTNA, Veronika et al. AFM-in-SEM as a tool for comprehensive sample surface analysis. *Microscopy Today*. 2020, vol. 28, no. 3, pp. 38–46.

62. VILANOVA-MARTÍNEZ, Paloma; HERNÁNDEZ-VELASCO, Jorge; LANDA-CÁNOVAS, AR; AGULLÓ-RUEDA, F. Laser heating induced phase changes of VO_2 crystals in air monitored by Raman spectroscopy. *Journal of Alloys and Compounds*. 2016, vol. 661, pp. 122–125.

SYMBOLS AND ABBREVIATIONS

PCF	Photonic crystal fiber
PM	Polarization maintaining
IPE	Institute of Physical Engineering
VFM	Vacuum fiber micromanipulator
SEM	Scanning electron microscope
LMA	Large mode area
TERS	Tip-enhanced Raman spectroscopy
AFM	Atomic force microscopy
CPEM	Correlative probe and electron microscopy
RGA	Residual gas analysis
BUT	Brno University of Technology
CEITEC	Central European Institute of Technology
IBAD	Ion beam assisted deposition
SPM	Scanning probe microscopy
LAO	Local anodic oxidation
pBN	Pyrolytic Boron Nitride